Cytoplasmic Colocalization of Granulins and TDP-43 Prion-like Domain Involves Electrostatically Driven Complex Coacervation Tuned by the Redox State of Cysteines.

Anukool A. Bhopatkar, Shailendra Dhakal and Vijayaraghavan Rangachari[$†].

Department of Chemistry and Biochemistry, School of Mathematics and Natural Sciences and [$]Center for Molecular and Cellular Biosciences, University of Southern Mississippi, Hattiesburg, MS 39406

[†] Corresponding author: Vijay Rangachari, 118 College Drive #5043, University of Southern Mississippi, Hattiesburg, MS 39406. Tel: 601-266-6044; email: vijay.rangachari@usm.edu

Running title: Liquid-liquid phase separation of Granulins and TDP-43

Key words: granulin, progranulin, TDP-43, FTLD, ALS, liquid-liquid phase separation, stress granules.

Abstract

Cytoplasmic inclusions containing aberrant proteolytic fragments of TDP-43 are associated with frontotemporal lobar degeneration (FTLD) and other related pathologies. In FTLD, TDP-43 is translocated into the cytoplasm and proteolytically cleaved to generate a prion-like domain (PrLD) containing C-terminal fragments (C25 and C35) that form toxic inclusions. Under stress, TDP-43 partitions into membraneless organelles called stress granules (SGs) by coacervating with RNA and other proteins. We were interested in understanding if and how cysteine-rich granulins (GRNs 1-7), which are the proteolytic products of a genetic risk factor in FTLD called progranulin, interact with TDP-43. We show that extracellular GRNs internalize and colocalize with PrLD as puncta in the cytoplasm of neuroblastoma cells but show no presence in SGs. In addition, GRNs and PrLD undergo liquid-liquid phase separation (LLPS) by complex coacervation, or form aggregates via liquid-solid phase separation (LSPS); the dynamics in these phase transitions appear to be driven by the negative charges on GRNs and fine-tuned by the positive charges and the redox state of cysteines. Furthermore, RNA competes with and expunges GRNs from GRN-PrLD condensates, providing a basis for GRN's absence in SGs. Together, the results bring to bear unique mechanisms by which GRNs could modulate TDP-43 proteinopathies.

Introduction

Frontotemporal lobar degeneration (FTLD), originally called Pick's disease, is a progressive neurodegenerative disease that affects the frontal and temporal lobes of patients predominantly 45-65 years of age (Bang, Spina, & Miller, 2015). The neuronal atrophy observed in these patients is associated with language impairments accompanied by behavioral and personality changes (Grossman, 2002; Seelaar, Rohrer, Pijnenburg, Fox, & van Swieten, 2011). Based on histopathological signatures, FTLD is subclassified into FTLD-TDP, FTLD-Tau, and FTLD-FUS (rare) (Bang et al., 2015; Irwin et al., 2015; Prasad, Bharathi, Sivalingam, Girdhar, & Patel, 2019). Nearly half of FTLD patients show the presence of neuronal and glial cytoplasmic inclusions of TAR DNA binding protein-43 (TDP-43) (Irwin et al., 2015) making FTLD-TDP a predominant category of the disease. Furthermore, 95% of sporadic amyotrophic lateral sclerosis (ALS) patients also show TDP-43 inclusions besides sharing common genetic etiologies with FTLD, making FTLD-TDP and ALS to be part of a clinicopathological continuum (Irwin et al., 2015). Molecular etiologies of familial FTLD are associated with mutations in microtubule-associated protein tau (*MAPT*) for FTLD-Tau and those in Progranulin (*GRN),* TDP-43 *(TARDBP)*, Fused in sarcoma (*FUS*), and Hexanucleotide repeat expansion in C9orf72 (*C9orf72*) for FTLD-TDP (Prasad et al., 2019; Seelaar et al., 2011; Sun & Chakrabartty, 2017).

TDP-43 is a 43 kDa protein that contains an N-terminal domain, two RNA recognition motifs (RRMs), and a prion-like, disordered, C-terminal domain enriched with low complexity sequences (PrLD) (François-Moutal et al., 2019; Prasad et al., 2019). Localized in the nucleus, TDP-43 is involved in a wide range of functions including transcriptional regulation, RNA metabolism, and splicing among others (Buratti & Baralle, 2008; Buratti et al., 2001; H. Y. Wang, Wang, Bose, & Shen, 2004). Under cellular stress such as heat shock, oxidative insults, inflammation (Herman Allison et al., 2019; Khalfallah et al., 2018) or nutrient starvation (Herman Allison et al., 2019), TDP-43 coacervates with mRNA and other proteins to undergo liquid-liquid phase separation (LLPS) and partitions into membraneless organelles called stress granules (SGs) (Khalfallah et al., 2018; Liu-Yesucevitz et al., 2010). SGs are reversible cytoplasmic assemblies formed in response to cellular stress to sequester and prevent mRNA transcripts from degradation or translation (Colombrita et al., 2009; Protter & Parker, 2016; Van Treeck et al., 2018). In pathological conditions, TDP-43 is translocated to the cytoplasm where it undergoes aberrant proteolytic cleavage to generate several C-terminal fragments (CTFs) of varying sizes including C35 (~35 kDa), C25 (~25 kDa), and C17 (~17 kDa) with the former two being the most abundant of them (L. M. Igaz et al., 2008; I. R. A. Mackenzie & Rademakers, 2008; Neumann et al., 2006; Y.-J. Zhang et al., 2009). These fragments are also known to be formed via alternative splicing to varying degrees (Xiao et al., 2015). Importantly, TDP-43 CTFs undergo aggregation to form toxic, insoluble inclusions in the cytoplasm which are the pathological hallmarks of ALS and FTLD patients (Lionel M. Igaz et al., 2009; Neumann et al., 2006). Despite the conspicuity of the TDP-43 CTF aggregates in patients, factors responsible for their biogenesis and subsequent roles in pathology remain poorly understood. Similarly, while the formation of biomolecular condensates is now well established for TDP-43 and other members of SGs such as hnRNP1 (Nunes et al., 2019; J. Wang et al., 2018), FUS (Nunes et al., 2019; Sama et al., 2013) and TIA1 (Gilks et al., 2004; Nunes et al., 2019), the link between SGs and amyloid formation for TDP-43 remains ambiguous, but one that could be key in neurodegenerative pathologies.

Another key protein implicated in FTLD is a 68.5 kDa secreted protein called progranulin (PGRN). The protein possesses pleiotropic functions including wound healing, tumorigenesis (Z. He & Bateman, 2003) and immunomodulation (Jian, Konopka, & Liu, 2013). In neurons, PGRN has been identified to play key roles in neuronal functions, lysosomal homeostasis, cell survival, and differentiation (Elia, Mason, Alijagic, & Finkbeiner, 2019; Gao et al., 2010; Gass et al., 2012; Zhiheng He & Bateman,

1999; Ryan et al., 2009; Tanaka et al., 2017; P. Van Damme et al., 2008), and has gained significant attention due to its link to neurodegenerative pathologies especially FTLD. About 30-50% of FTLD-TDP cases are of a heritable type with mutations in *GRN* underlying a majority of them (Chow, Miller, Hayashi, & Geschwind, 1999; van der Zee et al., 2007). The autosomal dominant heterozygous *GRN* mutations results in haploinsufficiency of the protein, which led to the conclusion that PGRN plays a neuroprotective role (Arrant, Onyilo, Unger, & Roberson, 2018; I. R. Mackenzie et al., 2011; Ward et al., 2017), while homozygous *GRN* mutations lead to neuronal ceroid lipofuscinosis (NCL), a lysosomal disease (Chitramuthu, Bennett, & Bateman, 2017; Ward et al., 2017). But for the genetic connection and haploinsufficiency, the precise mechanism by which PGRN may influence FTLD has not been established. In this context, the cysteine-rich, ~6 kDa modules called granulins (GRNs 1-7), which are the proteolytic products of PGRN (Zhu et al., 2002) have been of great interest to us for their potential roles in FTLD and other pathologies. It is now known that extracellular PGRN is endocytosed into the lysosome via a sortillin-mediated pathway to be processed by cathepsins into GRNs (C. W. Lee et al., 2017), which are thus speculated to possess lysosomal functions (Holler, Taylor, Deng, & Kukar, 2017; Root, Merino, Nuckols, Johnson, & Kukar, 2021). GRNs also function in a plethora of roles in normal cell biology (Park et al., 2011; Shoyab, McDonald, Byles, Todaro, & Plowman, 1990; Philip Van Damme et al., 2008) but possess opposing inflammatory properties to PGRN; while PGRN is anti-inflammatory, GRNs show pro-inflammatory properties (Zhu et al., 2002). During inflammation, PGRN secreted from activated microglia and astrocytes undergoes extracellular proteolysis by neutrophil elastases and other proteases to generate GRNs (Ungurs, Sinden, & Stockley, 2014). The fate of the extracellular GRNs on neuronal function and dysfunction remains unclear and we conjecture that they are taken up by neurons where they interact with TDP-43. Some support for this idea came from a report from Salazar and coworkers (Salazar et al., 2015) who showed that specific GRNs affected TDP-43 toxicity in a *C.elegens* model (Salazar et al., 2015). We also demonstrated that GRNs, 3 and 5, interact with and modulate the aggregation and phase behavior of TDP-43 PrLD *in vitro* (Bhopatkar, Uversky, & Rangachari, 2020). Furthermore, GRN immunopositivity observed in several regions of the brain in post-mortem Alzheimer disease and FTLD-TDP patients potentiates the significance of GRNs in pathology (Mao et al., 2017). Interestingly, acute inflammation has also shown to induce mislocalization and aggregation of TDP-43 in mice and cell culture (Correia, Patel, Dutta, & Julien, 2015), increasing the likelihood of its interaction with GRNs.

Here, we delve deeper into understanding the molecular factors that govern the interactions between GRNs and TPD-43 PrLD (termed PrLD hereafter). Our results show that extracellular GRNs-2, -3 and -5 internalize and colocalize with PrLD in the cytosol of neuroblastoma cells but do not partition into the SGs formed under stress with PrLD. In vitro experiments suggest that GRN-2 undergoes complex coacervation with PrLD to form liquid droplets in the oxidized state but promotes insoluble aggregates in the reduced state. Based on the empirical results from GRNs and their specifically designed mutations and chemical modifications, we conclude that the complex coacervation of GRNs and PrLD towards liquid droplet formation is driven by the negatively charged residues, while the increase in positively charged residues promote aggregation. Furthermore, we determine that the redox state of cysteines is a key modulator by fine-tuning liquid-liquid or liquid-solid phase separation of PrLD near counterbalancing electrostatic charge regimes. Additionally, we show that RNA displaces GRNs from the PrLD droplets that provides a possible reason for not observing GRNs within the SGs.

Results

GRN-2 colocalizes with TDP-43 PrLD in the cytoplasm but not in stress granules.

Unlike the GRNs generated in the lysosomes, the fate of those formed in the extracellular space remains unclear although transport to the cytosol has remained a possibility (Hoque, Mathews, & Pe'ery, 2010; Mao et al., 2017; Park et al., 2011). The ambiguity surrounding the precise localization of GRNs in pathophysiology has hindered understanding their roles in norm and pathology (Holler et al., 2017; Plowman et al., 1992). We conjecture that extracellular GRNs are internalized in the neuronal cytoplasm and potentially interact with proteolytic fragments of TDP-43 modulating the latter in ALS and FTLD patients. To recapitulate this scenario, we utilized a simple pulse-chase assay with fluorophore-labeled GRNs (Holler et al., 2017). In this assay, SH-SY5Y cells transiently expressing a blue fluorescence protein tagged PrLD construct (PrLD-SBFP2) were pulsed with media containing 500 nM of HiLyte532-labeled GRN-2 after 24 h (post-transfection), and then chased for an additional hour (see Methods). The cells were then imaged under non-stress and stress (with $NaAsO_2$) conditions (Fig 1). Under non-stress conditions, the transfected PrLD was observed in both the nucleus and cytoplasm (top panels; Fig 1a). Pulsing with GRN-2 showed internalization and colocalization with PrLD outside the nucleus (arrow; middle panels, Fig 1a). To see whether the colocalization was within or outside the lysosomes the cells were observed using a lysosomal marker which clearly indicted GRN-PrLD puncta outside the lysosomes (arrow; bottom panels, Fig 1a). Not surprisingly, to some degree, GRN-2 by itself was observed to be localized within the lysosomes as it is known to be present in them (yellow puncta; bottom panels, Fig 1a). Fluorescence recovery after photobleaching (FRAP) of the puncta showed no recovery of PrLD suggesting the formation of insoluble aggregates (green, top panel; Fig 1c). The samples were also immunodetected in the presence of TIA1 antibody, a key SG marker (Kedersha et al., 2000). In the non-stress conditions, TIA1 was located in the nucleus while PrLD had a disperse presence throughout the cell (Fig S1a). As expected, TIA-1 was absent from the colocalized PrLD and GRN-2 puncta as would be expected under non-stress conditions (No stress; Fig S1d). Under stress conditions induced by sodium arsenite, the transfected PrLD in SH-SY5Y cells showed puncta outside the nucleus (arrow; top panels; Fig 1b), consistent with SG formation (Colombrita et al., 2009; Khalfallah et al., 2018). Surprisingly, the fluidity of SGs observed by FRAP of PrLD did not show recovery (orange, top panel; Fig 1c), although widely varying photo bleaching recovery rates for SGs have been reported in cellular models (Gasset-Rosa et al., 2019; C. Wang et al., 2020; Wheeler, Matheny, Jain, Abrisch, & Parker, 2016). Nevertheless, PrLD's presence in SGs was confirmed by the colocalization of PrLD with TIA1 with a Meander's tM1 value of 0.59 (Fig S1b). Pulsing GRN-2 onto these

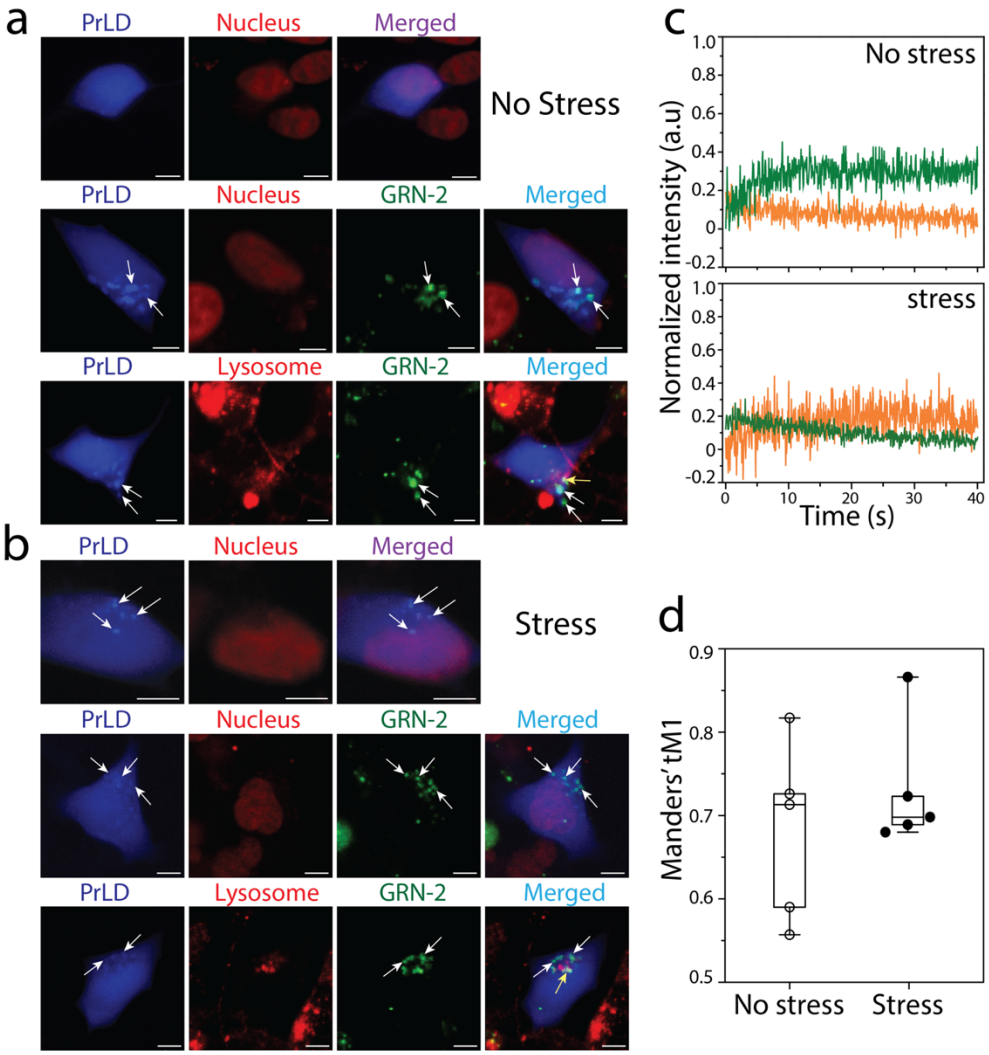

Figure 1. Cytoplasmic co-localization of GRN-2 and PrLD. Confocal microscopy images of live SH-SY5Ycells under homeostatic or stress conditions. a) Blue fluorescent protein tagged PrLD (PrLD-SBFP2) transiently expressed in SH-SY5Y cells alone and in the presence of Hilyte-532 labeled GRN-2 under non-stress conditions, and b) the same reactions under stress induced by sodium arsenite. White arrows indicate colocalized GRN-2 and PrLD puncta in the cytoplasm, while yellow arrows represent colocalization of GRN-2 in lysosomes (Scale bar= 5 µm). Visualization of nucleus and lysosomes were done by staining with NucSpot® Live 650 and Lysoview™ 650 respectively c) Normalized intensities of fluorescence recovery after photobleaching (FRAP) for puncta of PrLD alone (—) or colocalized PrLD-GRN-2 (—) in under non-stress (top) or stress (bottom) conditions. d) Whiskers plot of Manders' tM1 calculated for the colocalization of GRN-2 with PrLD using Fiji-ImageJ software. Each data-point represents the colocalization score of an independent cell.

cells under stress showed colocalization of both the proteins as puncta in the cytoplasm and outside the lysosomes (arrows; middle and bottom panels; Fig 1b). Here again, the colocalized puncta did not show fluorescence recovery (green, top panel; Fig 1c). Furthermore, GRN-2 did not show colocalization with TIA1 and PrLD suggesting that GRN-2 was not partitioned into the SGs (Fig S1d). In addition, two other GRNs known to modulate PrLD's phase transitions (Bhopatkar et al., 2020), GRNs 3 and 5, also did not

show colocalization with TIA1 under stress conditions, but colocalized with PrLD under both non-stress and stress conditions (Fig S1d-e). The colocalization of GRN-2 and PrLD was also statistically significant with ~ 73% of the internalized GRN-2 found to be colocalized with PrLD under stress and ~ 68% under homeostatic conditions (Fig 1d). The lack of fluorescence recovery observed for the truncated TDP-43 construct of PrLD within SGs could potentially suggest gelated material-like properties. To see if this is the case, SH-SY5Y cells were transfected with the full-length wild-type TDP-43 (wtTDP43tdTomato) as a control, which has been observed to being present within SGs with a full recovery upon photobleaching (Fig S2) (Gasset-Rosa et al., 2019). In our experiments too, FRAP showed the expected recovery of SGs as compared to the non-stress conditions (Fig S2), which suggests that SG assemblies containing PrLD construct may indeed possess solid- or gel-like characteristics. Taken together, the data establish that extracellular GRN-2 internalizes and colocalizes with PrLD in the cytoplasm but is not present within the SGs.

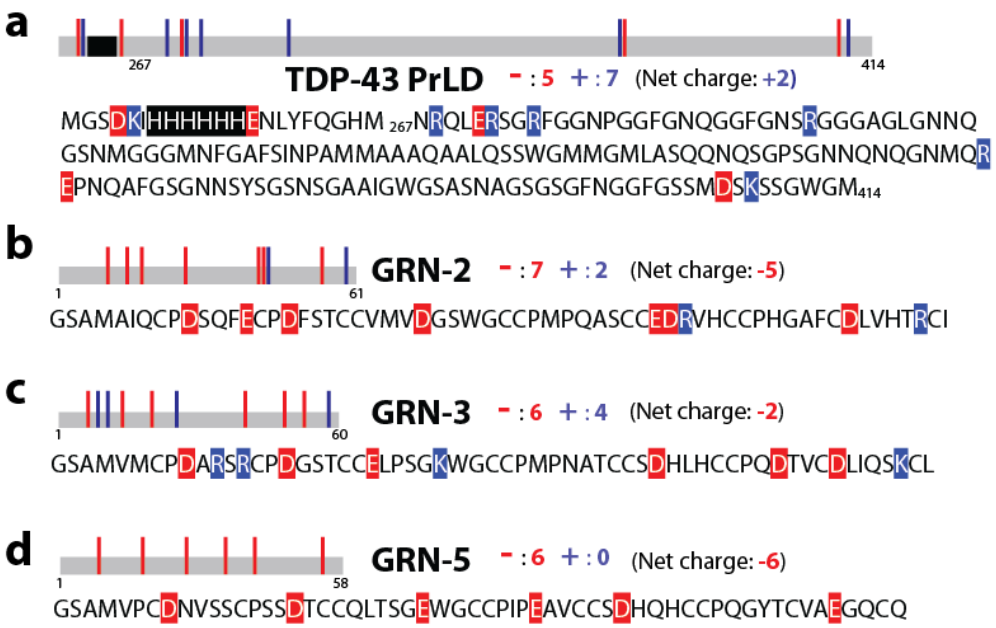

Figure 2. Sequences of granulins (GRNs) and TDP-43 under investigation. a) TDP-43 PrLD construct (residues 267-414) along with a hexa-histidine tag (highlighted) used in the study. b-d) Sequences of GRN-2 (b),-3 (c) and -5 (d). Sequences of proteins are annotated with acidic (red) and basic (blue) residues, along with the net charges on the respective proteins at neutral pH.

GRN-2 modulates the phase transitions of PrLD *in vitro*

The observation of cytoplasmic puncta of colocalized PrLD and GRN-2 decoupled from SGs, prompted us to investigate their interactions in greater detail. TDP-43 is known to undergo dynamic phase transitions depending on the cellular conditions to form either liquid condensates or solid aggregates (Ciryam et al., 2017; Fang et al., 2019; Watanabe et al., 2020). Understanding the molecular grammar of protein LLPS has revealed that weak, multivalent interactions between 'stickers' involving electrostatics, π-π (between tyrosines) or cation- π (between aromatic residues and arginines and lysines) that are separated by scaffolds called 'spacers' (Choi, Dar, & Pappu, 2019; Choi, Holehouse, & Pappu, 2020; J. Wang et al., 2018), are the main driving forces of condensate formation. Disordered proteins enriched in one kind of charge will repel one another preventing self-coacervation but interaction with a partner

229 containing counter-charge would minimize repulsion and promote LLPS (Pak et al., 2016). These
230 interactions are also observed to be the driving forces behind the self- and complex- (with RNA)
231 coacervation of TDP-43 (Babinchak et al., 2020; Conicella, Zerze, Mittal, & Fawzi, 2016; Li, Chiang,
232 Chou, Wang, & Huang, 2018). However, the molecular determinants of heterotypic phase transitions of
233 TDP-43 involving ligands vary depending on the partners and are still being discerned (Babinchak et al.,
234 2020). Despite the lack of a canonical RNA binding domain, TDP-43 PrLD undergoes complex
235 coacervation with RNA, which illustrates the prominence of aforementioned interactions in phase
236 separation (Bhopatkar et al., 2020; Conicella et al., 2016; Lim, Wei, Lu, & Song, 2016). However, the
237 phase transitions are dictated by the balance between weak, multivalent interactions that drive LLPS, and
238 strong, high affinity interactions that mediate liquid-solid phase separation (LSPS) often observed among
239 amyloid proteins. Our earlier investigations into the interactions of PrLD with GRN-3 and GRN-5
240 showed that GRN-3 induces LSPS in both oxidizing and reducing conditions, while GRN-5 undergoes
241 LLPS by complex-coacervation with PrLD (Bhopatkar et al., 2020). We conjecture that the disparity in
242 the behavior of GRNs is due to the high net negative charge on GRN-5 (– 6; six – and no + charges, Fig
243 2d) as opposed to GRN-3 (– 2; seven – and two + charges, Fig 2c) that counter-interact with PrLD's net
244 charge (+2) (Fig 2a). It is also likely that the lack of positive charges on GRN-5 plays a role. Here, we
245 extended these investigations to uncouple the molecular determinants of the complex coacervation by
246 investigating GRN-2. All three GRNs, 2, 3, and 5 possess a similar number of negatively charged acidic
247 residues (7, 6, and 6 respectively, Fig 2b-d) but vary in the number of positively charged basic residues
248 (2, 4, and 0, respectively, Fig 2b-d), making GRN-2 ideal to investigate. The presence of structural
249 disorder in proteins is known to be an implicit contributor to LLPS (Brangwynne, Tompa, & Pappu,
250 2015; Majumdar, Dogra, Maity, & Mukhopadhyay, 2019; Muiznieks, Sharpe, Pomès, & Keeley, 2018;
251 Uversky, 2017; Wright & Dyson, 2015); PrLD is largely a disordered region of TDP-43 while GRN-2 is
252 also predicted to be disordered in the fully reduced state by IUPred2A platform (Fig S3a-b) (Erdős &
253 Dosztányi, 2020; Mészáros, Erdos, & Dosztányi, 2018). This prediction was confirmed by biophysical
254 characterization of GRN-2 which revealed a structure dominated by random coils in both redox-forms
255 (Fig S4a), similar to GRNs 3, and 5 (Bhopatkar et al., 2020) (Fig S3c-d and S4e).
256 To probe the ability of GRN-2 in both redox forms to modulate phase transitions of PrLD, 40 μM
257 GRN-2 (oxidized form) or rGRN-2 (reduced form) were mixed with 20 μM PrLD buffered in 20 mM
258 MES, pH 6.0 and the samples were visualized by differential interference contrast (DIC) microscopy (Fig
259 3a-c). Immediately upon coincubation of GRN-2 and PrLD, the sample phase separated into liquid
260 droplets ranging between 2 and 12 μm diameter (Fig 3a). The droplets also showed classic wetting
261 behavior suggestive of their liquid-like characteristics (arrow; Fig 3b). The colocalization of proteins
262 within the droplets was confirmed using orthogonal fluorophores, HiLyte405 (blue) and HiLyte647 (red)
263 for GRN-2 and PrLD, respectively, as well as their liquid-like properties by coalescence and fusion of
264 droplets (Fig 3b). In stark contrast, samples containing rGRN-2 and PrLD showed the formation of solid
265 insoluble aggregates (Fig 3c) which also involved colocalization of both proteins (Fig 3d). These results
266 indicate that GRN-2 in the oxidized form induced LLPS of PrLD, while the reduced form induced LSPS.
267 Treatment of GRN-2-PrLD droplets with 1,6-hexanediol (HD), an agent that is known to disrupt weak
268 hydrophobic interactions and dissolve droplets (Düster, Kaltheuner, Schmitz, & Geyer, 2021; Shulga &
269 Goldfarb, 2003), showed persistence of the condensates even after treatment (top panels; Fig 3e) but with
270 a ~ 40% reduction in the turbidity levels compared to pre-HD treated sample suggesting that some
271 hydrophobic interactions contributed to LLPS. Similar treatment of HD to PrLD-RNA coacervates
272 showed a ~25% decrease in turbidity reaffirming that LLPS involving the two was driven primarily by
273 electrostatic interactions (middle panels; Fig 3e). In contrast, LLPS of PrLD induced by salt showed as

much as 90% of droplets dissolved with HD treatment (bottom panels; Fig 2e). Together, the data indicate that the coacervation of GRN-2 and PrLD is likely driven largely by electrostatic interactions.

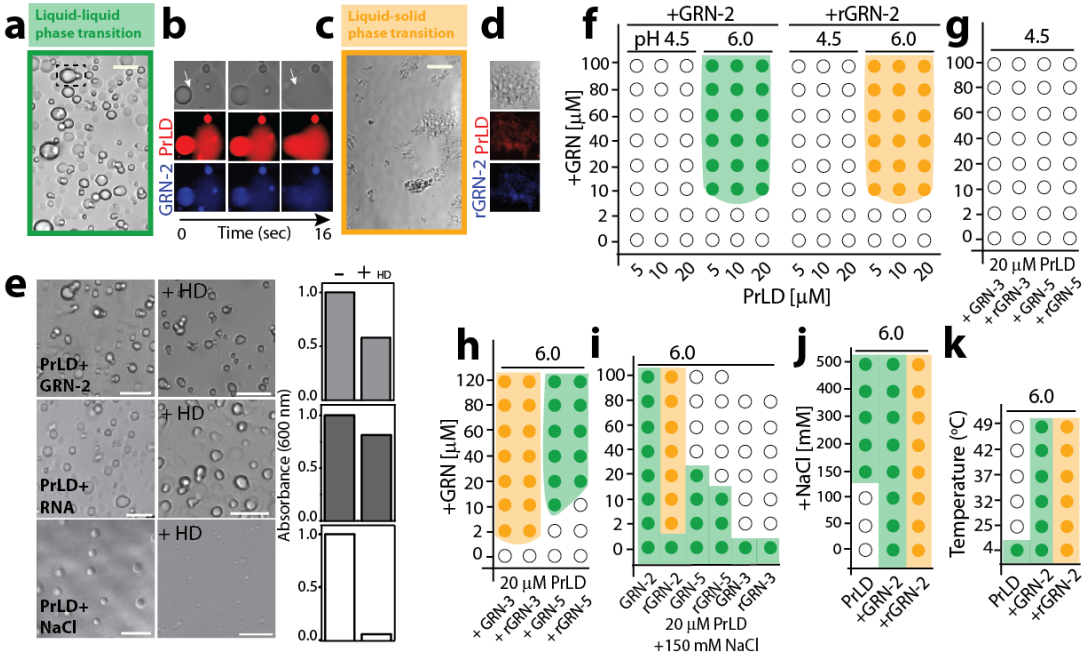

Figure 3. Phase transitions involved in GRN–TDP-43 PrLD interactions. a-d). DIC microscopy images of a mixture containing 20 μM PrLD with 40 μM fully oxidized GRN-2 (a-b) or reduced rGRN-2 (c-d) in 20 mM MES, pH 6.0. GRN-2 undergoes LLPS with PrLD (highlighted with green box) that shows the coalescence of droplets (a, dashed box) while rGRN-2 undergoes LSPS (saffron box). GRN-2 or rGRN-2 labelled with HiLyte 405 (blue) and PrLD with HiLyte 647(red) were visualized using confocal fluorescence microscopy which shows fusion of droplets for GRN-2 (white arrow; b) and deposition of solid aggregates for rGRN-2 (d). e) A mixture containing 40 μM GRN-2 with 20 μM PrLD was treated with 1,6-hexanediol (HD) to monitor its effect on the LLPS of the proteins which were quantified using OD_{600} pre- and post- HD treatment. Similar treatment was performed for condensates of 20 μM PrLD with either RNA (50 μg/mL) or NaCl (150 mM). The turbidity values were normalized with respect to their values pre-HD treatment. f) Phase diagram for GRN-2 or rGRN-2 with PrLD generated by varying the pH (buffered with 20 mM ammonium formate at pH 4.5 or 20 mM MES at pH 6.0) and concentrations of the respective proteins. g-h) Phase diagram for varying concentrations of GRN-3 and GRN-5 with 20 μM PrLD at pH 4.5 (g) and pH 6.0 (h). i) Turbidity assay performed by titrating the self coacervates of 20 μM PrLD (generated in presence of 150 mM NaCl) with increasing concentrations of GRN-2, GRN-3 or GRN-5. j) Titration of complex coacervates of 20 μM PrLD (generated with 40 μM GRN-2 or rGRN-2) with increasing concentration of NaCl (50-500 mM). k) The turbidity of 20 μM PrLD alone, or in presence of 40 μM GRN-2 or rGRN-2 measured as a function of temperature. The phase boundaries were established by considering an OD_{600} value of 0.14 as a cut-off for phase transitions. Scale bar represents 10 μm.

Then LLPS or LSPS phase boundaries were determined for GRN-2 and rGRN-2 with PrLD using turbidimetric assays (Fig 3f-k). In all these experiments, LLPS and LSPS were differentiated based on microscopic examination of the samples and phase boundaries established by considering an OD_{600} value of 0.140 a.u. as a cut-off for phase transitions (see Methods). To see if the negative charges drive GRN-PrLD LLPS, phase separation was observed at two different pHs; at pH 6.0 where the acidic residues have a net negative charge and at pH 4.5 where the acidic residues are close to being neutral. At pH 4.5,

no phase separation was observed for GRN-2 or rGRN-2 with PrLD (Fig 3f, pH 4.5) but at pH 6.0, the proteins underwent phase transitions uniformly at concentrations of 10 μM GRN-2 or rGRN-2 in all PrLD concentrations tested (Fig 3f, pH 6.0). However, in stark contrast, under fully reducing conditions, co-incubations of rGRN-2 with PrLD showed LSPS. The phase diagrams of GRN-3, GRN-5 with PrLD reveal both similarity and disparity in their phase transitions as previously observed (Bhopatkar et al., 2020)(Fig 3g-h); In an acidic environment, neither GRN undergoes phase transition with PrLD (Fig 3g) similar to GRN-2. At pH 6.0, both oxidized and reduced forms of GRN-3 show LSPS exclusively, albeit with a delay (solid precipitates observed after ~24 h), while incubation with GRN-5 showed LLPS exclusively (Fig 3h) (Bhopatkar et al., 2020). Together, these results suggest that the negatively charged residues on GRNs (evident from GRN-5, and data from assays at pH 4.5) are significant contributors of the complex coacervation with PrLD while an increasing number of positive charges on the protein modulates the dynamics towards LSPS (as observed from GRN-2 and GRN-3). Furthermore, we also questioned if and how GRNs modulate the self-coacervation of PrLD in presence of 150 mM NaCl (Fig 3i). Under oxidizing conditions, GRN-2 did not alter PrLD LLPS even at high concentrations whereas, under reducing conditions, rGRN-2 induced LSPS even at ten-fold lower stoichiometry (Fig 3i). Both redox forms of GRN-5 attenuated the phase transitions of PrLD at high concentrations suggesting a net repulsive interaction (Fig 3i). The attenuation of LLPS under reducing conditions could be attributed to the formation of hydrogen bonds from the free thiols (12 in GRNs) to polar residues (Ser, Asn) on PrLD, that results in stronger solute-solute interactions and concomitant LSPS. To further observe the effect of electrostatics on phase transitions, the effect of increasing salt concentrations was probed (Fig 3j) on the process. As observed previously (Bhopatkar et al., 2020), PrLD alone failed to phase separate below physiological salt concentrations (up to 150 mM NaCl). On the other hand, upon co-incubation with GRN-2, PrLD showed LLPS well below physiological salt concentrations while in the presence of rGRN-2 LSPS was observed (Fig 3j). The increasing salt concentration had no significant effect on phase transitions of PrLD co-incubated with either redox form of GRN-2, but an increased magnitude of phase separation was observed indicating the simultaneous presence of homo- and heterotypic condensates of PrLD within the sample (data not shown). Finally, the temperature dependence of PrLD-GRN-2 phase transitions was examined to establish the upper critical solution temperature (UCST) (Conicella et al., 2016; H. R. Li et al., 2018). As expected PrLD underwent self-coacervation in no salt conditions at 4°C that was attenuated at 25 °C and above suggesting a UCST between these temperatures (Fig 3k). Co-incubation with GRN-2 increased UCST to > 49 °C, while the sample with rGRN-2 showed LSPS in all the temperature range recorded (Fig 3k).

Negatively charged residues in GRNs drive LLPS while the positively charged ones enhance LSPS.

The pH dependence on phase transitions (Fig 3f) provided an important clue regarding the involvement of electrostatic interactions, especially the negatively charges residues. To further investigate these aspects, the phase behavior of the three granulins, GRN-2, -3, and -5 along with specific mutants of GRN-2 were investigated. As mentioned above, all three GRNs are isoelectronic with respect to the negative charges (-7, -6, and -6, respectively) but contain a varying number of positively charged residues (2, 4 and 0, respectively) (Fig 2). As previously shown (Bhopatkar et al., 2020), microscopic investigations of GRN-3 incubated with PrLD in both redox states showed LSPS (saffron box) while GRN-5 showed LLPS (green box) under both redox conditions (Fig 4a and b). FRAP confirmed the observations with a rapid recovery for GRN-5 (liquid) and attenuated recovery for GRN-3 (solid) (Fig 4a and b). On the other hand, GRN-2 showed LLPS in the oxidized state and LSPS in the reduced state (Fig 4c). This suggests that the number of positive charges in GRN-2 is enough to mitigate LLPS in the

reduced state but not enough to attenuate LLPS and promote LSPS in the oxidized state. We conjectured that while negative charges on the GRNs promote LLPS, the positively charges residues tend to shift the equilibrium towards LSPS and solid aggregates. To further substantiate the role of positive charges, a construct was generated in which the two positive charges were mutated to glutamate (negatively charged) residue to generate GRN-2 (+/-) mutant that was devoid of any positive charges (net - 9 charge) similar to GRN-5. If our hypothesis was correct, abrogation of all positively charged residues would promote LLPS in both oxidized and reduced states identical to GRN-5. Co-incubation of GRN-2 (+/-) and PrLD did show formation of liquid droplets in both fully oxidized and reduced conditions (Fig 4d), further cementing our hypothesis that negative charges drive LLPS. To further illustrate this, GRN-7, which has the same number of acidic (-6) residues as the other GRNs but has high number of basic residues (+8), with an overall positive charge (+2), was co-incubated with PrLD (Fig S5a). Based on the on the inferences drawn thus far, such enrichment of positively charged residues will drive LSPS of PrLD, which was confirmed by the presence of solid aggregates on the co-incubated sample monitored for 36 h (Fig S5c). Unfortunately, a deeper investigation on this protein was precluded by the difficulties in obtaining a pure protein that was prone to substantial proteolytic degradation over time (data not shown). Lastly, we evaluated the droplets formed by these proteins with PrLD (Fig S8). The droplet area (μm^2) of GRN-2 with PrLD shows a normal distribution centered at ~25 μm^2 (Fig S8, gray), which is similar to that observed for GRN-2(+/-) with PrLD (Fig S8, red). On the other hand, droplets formed in the reaction of rGRN-2(+/-) with PrLD shows noticeable reduction in droplet areas with a normal distribution centered at ~10 μm^2, suggesting an diminished ability of the reduced form to undergo LLPS.

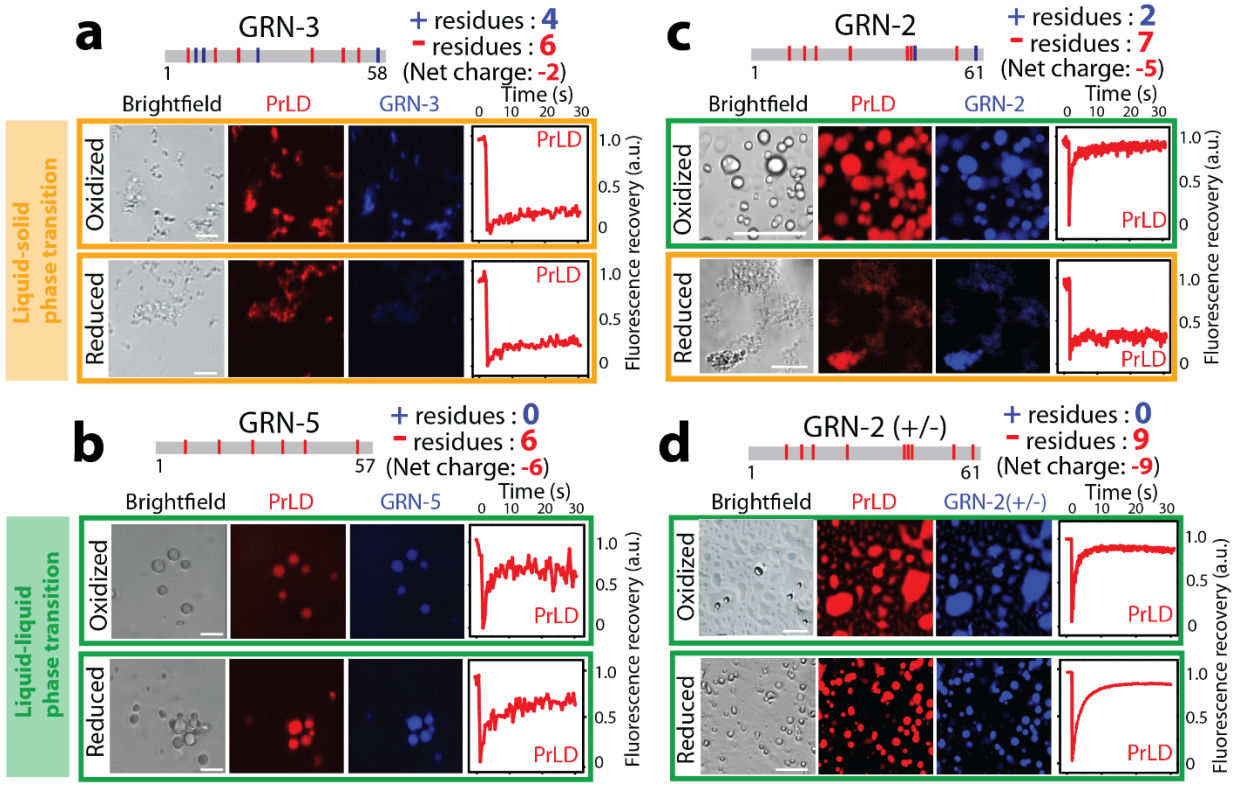

Figure 4. Phase transitions of GRNs and specific mutants. a-d) Sequence of GRN-3, GRN-5, GRN-2 and GRN-2(+/-) annotated with negative and positive charges present and the net charges on the protein at neutral pH (top of each panel). Individual samples are generated by mixing 40 μM of the respective GRN

with 20 μM PrLD, along with 1% (molar) fluorophore-labeled proteins (GRNs are labeled with HiLyte-405 and PrLD with HiLyte 647) buffered in 20 mM MES, pH 6.0. Samples were visualized by fluorescence microscope and their internal dynamics were analyzed by FRAP. Individual micrographs are highlighted with a green border for LLPT and a saffron border for LSPT. The fluorescence recovery curves were normalized based on pre-bleaching fluorescence intensities. Scale bar represents 10 μm.

The redox state of cysteines in GRNs further tunes phase behavior of PrLD coacervates.

It is now clear that the complex coacervation of GRN and PrLD is driven predominantly by electrostatic interactions; while negative charges drive LLPS the increase in the number of positive charges shift the equilibrium towards LSPS. However, what role does the oxidation state of thiols play in this process remained unclear. Therefore, to understand their effect, microscopic analysis was performed on the co-incubations of GRN-2 and PrLD as a function of a reducing agent (Fig 4). To mimic local redox fluxes within the cellular cytoplasm (López-Mirabal & Winther, 2008), the reactions containing 40 μM GRN-2 and 20 μM PrLD with increasing concentrations (50-600 μM) of the reducing agent tris(2-carboxyethyl)phosphine (TCEP) were probed using fluorescence microscopy (Fig 4a). The TCEP concentrations used generate partially reduced (50-300 μM) to completely reduced (600 μM) thiols in GRN-2. In the absence of the reducing agent, GRN-2, as expected, underwent LLPS with PrLD forming liquid droplets that undergo fusion and coalescence as observed previously (0 μM TCEP; Fig 5a). To ascertain the droplets' fluid-like properties, their internal dynamics were probed by FRAP which showed a rapid recovery for PrLD reiterating an archetypal fluidic characteristic of the droplets (red curve, 0 μM TCEP; Fig 5a). For reasons not clear at this time, attenuated mobility for the colocalized GRN-2 within the liquid droplets was observed as seen in its recovery curve, (blue curve, 0 μM TCEP; Fig 5a).

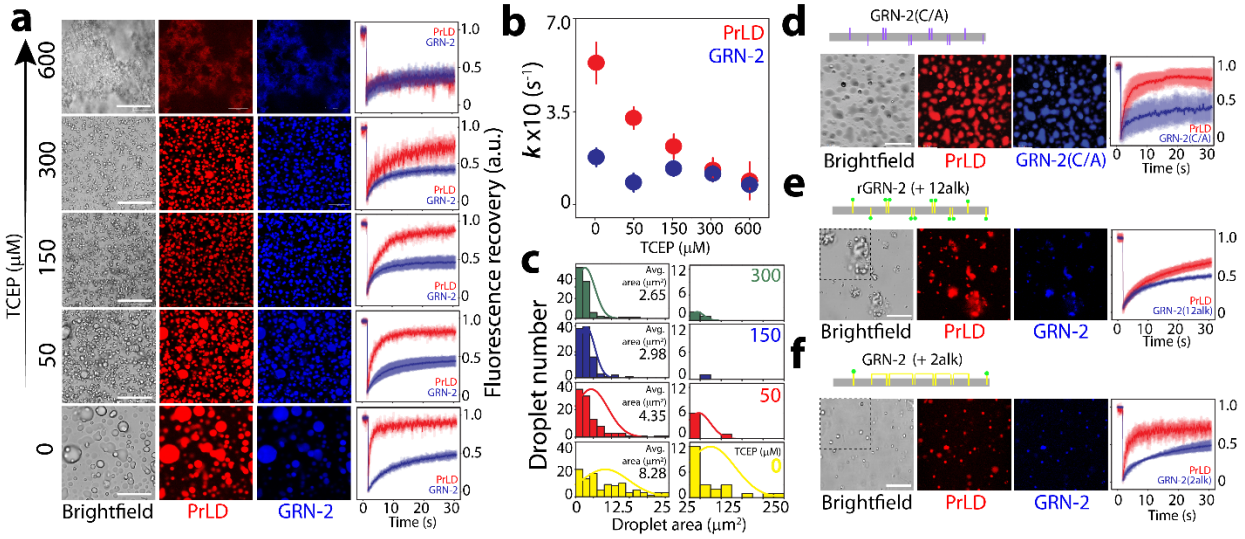

Figure 5. Redox state of GRN-2 fine tunes the phase transitions with PrLD. a) Reactions containing 20 μM PrLD with 40 μM GRN-2 were initiated separately with increasing TCEP concentrations (50-600 μM) buffered in 20 mM MES, pH 6.0. Samples were visualized by fluorescence microscopy and probed with FRAP. b) Individual recovery rates of PrLD (red) and GRN-2 (blue) in the reactions of a) obtained using the initital rate method (detailed in Materials and Methods). c) Distributions of droplet area (μm^2) observed within the micrographs of reactions in (a). The droplet area distributions were extracted using ImageJ where a total of 100 droplets was considered for each sample and Normal distribution are plotted (detailed in Materials and Methods). d) Schematic depicting the GRN-2(C/A) mutant (cysteines replaced with alanines;

402 purple vertical bars). The micrographs represent reactions of 20 μM PrLD with 40 μM GRN-2(C/A)
403 buffered in 20 mM MES, pH 6.0 along with the FRAP analysis. e-f) Micrographs of mixtures containing
404 40 μM alkylated-GRN-2 (e; 2-free thiols alkylated, f; 12-free thiols alkylated) generated using
405 iodoacetamide, with 20 μM PrLD along with the FRAP analysis. For visualization using fluorescence
406 microscopy, all samples contained 1% fluorophore-labeled proteins (GRN-2, GRN-2(C/A), and alkylated
407 forms were labeled with HiLyte-405 while PrLD was labeled with HiLyte-647). All reactions were initiated
408 and imaged at room temperature. Scale bar represents 20 μm.

409 In the presence of 50 μM TCEP (partially reducing conditions), the magnitude of droplet formation
410 was dampened and structures with an altered morphology alongside the spherical droplets were visible
411 (50 μM TCEP; Fig 5a). Increasing concentrations of TCEP (150-600 μM) showed smaller droplets and a
412 progressive decrease in fluorescence recovery rates for PrLD (Fig 5a and 5b). The rate constant (*k*)
413 deduced by an initial rate method from FRAP data showed a first-order kinetics for PrLD, while GRN-2
414 showed a diminished rate of recovery in fully oxidized and partially reduced (50 μM TCEP) conditions
415 (Fig 5b). In fully reducing conditions, the mixture of rGRN-2 and PrLD underwent LSPS, as observed
416 previously (Figs 3 and 4) generating solid, fibril-like aggregates and was devoid of any droplets, as
417 confirmed via microscopy and FRAP data (600 μM TCEP; Fig 5a). The use of other reducing agents such
418 as dithiothreitol (DTT) and glutathione (GSH) also showed similar results (Fig S6). Furthermore, analyses
419 of droplet size as a function of the reducing agent provided some interesting insights (Fig 5c). The droplet
420 size distributions, in terms of the surface area, were clubbed into two categories of small (area < 25 μm^2)
421 and large droplets (25 < area < 250 μm^2). The coacervates in fully oxidized conditions showed a wide
422 distribution of droplet sizes. The surface areas of small droplets were centered at ~10 μm^2, with an
423 average droplet size of 8.2 μm^2 (yellow; Fig 5c). In addition, a notable number of droplets larger than 25
424 μm^2 were also observed in the sample with an average surface area of ~ 60-70 μm^2 (yellow; Fig 5c).
425 Increasing TCEP concentrations (50-600 μM) revealed a discernible shift towards smaller droplet
426 distributions with average surface areas of 4.35, 2.89 and 2.65 μm^2 for 50, 150, and 300 μM TCEP
427 concentrations, respectively (Fig 5c). We attribute this behavior to the reduction in surface tension
428 introduced by way of thiols solvation or hydrogen bonding interactions.

429 These results bring out two important points; the first is that the modulation of phase transitions by
430 redox flux is not abrupt but requires full reduction of cysteines to shift the droplets (LLPS) to insoluble
431 aggregates (LSPS). The second is that the cysteine thiols seem to shift the equilibrium from the liquid to
432 the solid phase possibly indulging in hydrogen bonding interactions with bulk water (solvation) and with
433 PrLD. If this is the case, we argued that abrogation of cysteines (and therefore, thiols) will render GRN-2
434 to behave as in fully oxidizing conditions. To test this hypothesis, all 12 cysteines in GRN-2 were
435 mutated to alanines to generate GRN-2(C/A) mutant. Indeed, the co-incubation of PrLD with GRN-
436 2(C/A) immediately showed LLPS to form liquid droplets with high rates of fluorescence recovery
437 confirming a fluid-like character (Fig 5d). The similarity in the behavior of GRN-2(C/A) and GRN-2 is
438 also appratent from the droplet size observed (Fig S8). The droplet areas of the mutant form (Fig S8,
439 green) have a similar distribution to that of the wild type (Fig S8, gray), with an average value of ~25
440 μm^2. On the contrary, when all the free thiols in the fully reduced form of rGRN-2 were alkylated and
441 capped with acetamide (GRN-12alk), a moiety, which is expected both to be solvated by bulk water and
442 engage in hydrogen bonding interactions with PrLD perhaps to a greater extent than thiols, the
443 coacervates formed solid like structures with attenuated internal mobility as revealed by FRAP (Fig 5e).
444 Similarly, acetamide alkylation of two free thiols present in the fully oxidized samples (Fig S4), which
445 mimics partially reducing conditions also showed no change from those incubated in the presence of 50

μM TECP (Fig 5f). Together, the data bring to light the role of cysteine in phase transitions of PrLD and GRNs, which is one of modulatory nature, fine-tuning the transitions only GRN-2, which happens to fall in category of partially counter-balanced positive and negative charges. As observed before (Bhopatkar et al., 2020), GRNs 3 and 5 showed no effect on respective phase transitions due to the extremity of the electrostatics in their respective cases.

GRN-2 delays but induces ThT-positive aggregates of TDP-43 PrLD in oxidized or reduced states.

We have previously shown the concentration-dependent LLPS of PrLD by GRN-5 or LSPS by GRN-3 are accompanied by a delayed emergence of thioflavin-T (ThT) fluorescence (Bhopatkar et al., 2020), which is a reporter of amyloid-like aggregates (Xue, Lin, Chang, & Guo). To see whether GRN-2 in both redox forms induces ThT-positive PrLD aggregates, the co-incubations of increasing concentrations of GRN-2 or rGRN-2 and PrLD were monitored for 24 hours in the presence of ThT (Fig 6a). All reactions showed slightly elevated ThT levels at the beginning (0h; Fig 6a) but failed to show sigmoidal increase of ThT fluorescence as observed for the control PrLD (Fig 6a). This observation was similar to that observed previously with GRN-3 and GRN-5 (Bhopatkar et al., 2020). Microscopic investigations of the reactions with GRN-2 showed the formation of liquid droplets in all stoichiometric equivalence immediately after incubation (0h; Fig 6b). After 24h, the droplets continue to be present although a few of them showed morphological changes possibly gelation (24h; Fig 6b). To probe this possibility, we performed FRAP studies on the structures after a 24h period. Compared to the fluorescence recovery shown by the liquid droplets of 40 μM GRN-2 with 20 μM PrLD (Fig 6b, FRAP, 0 h; red), the distorted droplets visible in samples of all stoichiometric reactions, show attenuation in their recovery kinetics (Fig 6b, FRAP, 24 h; brown) confirming the 'gelation' of the liquid-like droplets observed initially. Also, this attenuation shows a positive correlation to the concentration of GRN-2 present in the mixture. In fully reducing conditions, incubations of rGRN-2 with PrLD showed an instantaneous formation of insoluble aggregates that persisted after 24 h (Fig 6c). However, after > 60 hours of incubation, all the reactions with rGRN-2 and those with GRN-2 in lower stoichiometric equivalence showed increases in ThT intensities towards amyloid like materials (Fig S6).

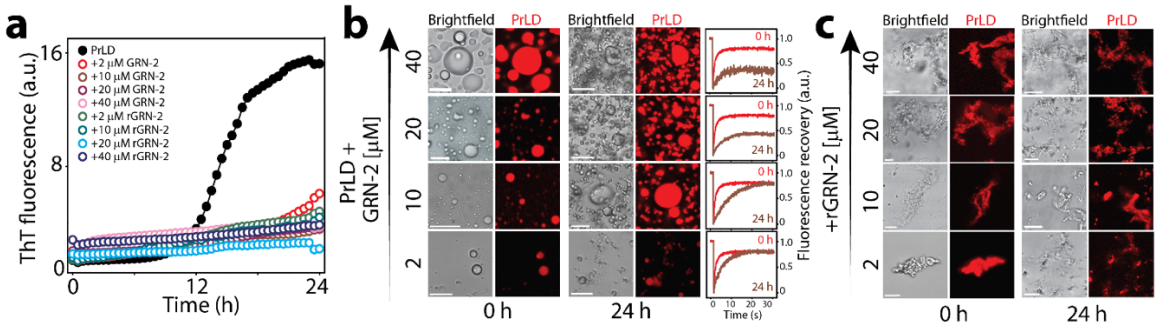

Figure 6. Amyloid formation of PrLD in presence of GRN-2. a) The amyloid formation of 20 μM TDP-43 PrLD alone (●) or in presence of varying concentrations (2-40 μM) of GRN-2 or rGRN-2, buffered in 20 mM MES, pH 6.0, monitored using 15 μM ThT for a period of 24 h at 37 ºC under quiescent conditions. b-c) Micrographs of reactions in (a) visualized using brightfield and fluorescence microscope with 1% fluorophore-labeled PrLD (HiLyte-647) imaged at 0 h and after an incubation of 24 h. b) The droplets observed initially upon mixing GRN-2 with 20 μM PrLD were subjected to FRAP analysis immediately and after 24 h (0 and 24 h, red and brown curves, respectively). c) Microscopic visualization of PrLD in the

presence of varying concentrations of rGRN-2 (2-40 μM) shows the formation of solid deposits at 0 h and 24 h. Scale bar represents 10 μm.

RNA competes and displaces GRN-2 from PrLD coacervates.

Under cellular stress conditions, PrLD transfected in SH-SY5Y cells is either found in SGs along with TIA1 or colocalized with GRNs in the cytoplasm but colocalization of all three was not observed (Fig S1). We conjectured that it is due to potential competition between GRNs and RNA, in which the latter displaces the former in SGs. To test this, ternary interactions between RNA, GRN-2, and PrLD were investigated in vitro (Fig 7). PrLD (20 μM) was co-incubated with three GRN-2 concentrations of 10, 20 and 40 μM, and each co-incubated sample was investigated with the addition of increasing RNA (poly A) concentrations (0-150 μg/mL). The positive control, PrLD, and RNA showed prototypical turbidity increase increasing RNA concentrations that saturated about 50 μg/mL and showed a slight drop in turbidity at 150 μg/mL (●; Fig 7a). Increasing RNA concentrations in PrLD-GRN-2 co-incubations also showed similar trends but with higher initial turbidity values (●,●, and ●; Fig 7a). Irrespective of the concentration of GRN-2 in the mixture, the eventual turbidity values of all samples converge to that shown by PrLD with 150 μg/mL RNA. This hints at the similar compositional make-up of the final condensates which is insensitive to GRN-2 concentration in the presence of high RNA concentration (Fig 7a). To probe the internal dynamics of these interactions, we used fluorescence microscopy with fluorophore-labeled proteins and repeated the experimental setup. Co-incubations of varying concentrations of GRN-2 with PrLD, in the absence of RNA, showed droplet formation as expected (0 RNA; Fig 7b-e). The addition of increasing amount of RNA to 10 μM GRN-2 incubations showed a steady displacement of GRN-2 (blue) from within the droplet from ~ 50-75 μg/mL, while PrLD (red) remained largely unaffected (Fig 7c). Between 100 and 150 μg/mL of RNA, GRN-2 has been completely displaced from the droplet (Fig 7c). Interestingly, the displacement and substitution of GRN-2 did not occur concertedly but involved the formation of heterologous coexisting multiphase condensates with coacervates of PrLD-RNA engulfing PrLD-GRN-2 as deduced by the fluorescence intensity plots (Fig 7c).

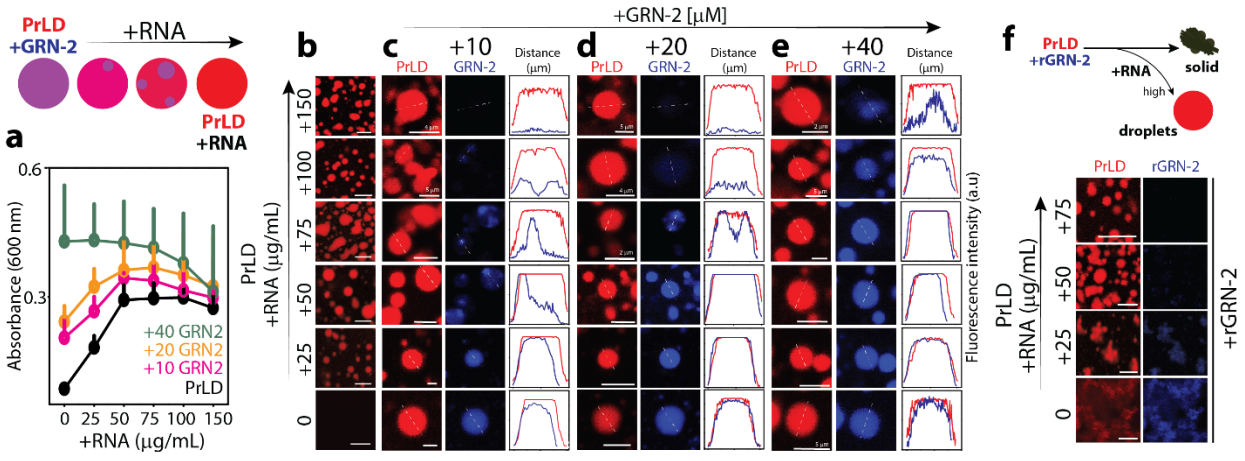

Figure 7. Ternary interactions between GRN-2, PrLD and RNA. a) Turbidity plots obtained by titrating 20 μM PrLD with increasing RNA concentration (25-150 μg/mL) in the presence (●; 10 μM , ●; 20 μM or ●;40 μM GRN-2) or the absence of GRN-2 (●). b-e) Confocal micrographs depicting selective droplets observed in reactions from (a). Displacement of GRN-2 upon titration with RNA was observed by the

fluorescence intensity profiles of the respective fluorophore-labeled proteins (GRN-2 with HiLyte-405 and PrLD with HiLyte-647) was extracted across the width of the droplets using ImageJ (detailed in Materials and Methods). f) Microscopic visualization of complex coacervates of 20 μM PrLD with varying RNA concentrations (25-75 μg/mL) generated initially were titrated with 40 μM rGRN-2. All reactions were intiated and imaged at room temperature. Unless specified, scale bar represents 10 μm.

A similar behavior was observed with increased GRN-2 concentrations (20 and 40 μM) also (Fig 7d-e). Such co-existing heterotypic condensates have also been observed in ternary complexes involved in prion-like polypeptide, RNA and arginine-rich polypeptides (Kaur et al., 2021). Similar to Kaur and colleagues, we observe a ternary system in which RNA-PrLD interactions out compete and dominate PrLD-GRN-2 interactions by displacing GRN-2. This also suggests that GRN-2 and RNA are mutually exclusive binding partners for PrLD demixing and LLPS, which in turn explains why GRN-2 are not observed in SGs. Furthermore, we also examined the effect of rGRN-2 on the condensates of PrLD-RNA was also examined (Fig 7f). Here, condensates of 20 μM PrLD with varying RNA concentrations (25-75 μg/mL) were generated and 40 μM rGRN-2 was added followed by visualization using fluorescence microscopy. We observed that at a low RNA concentration (25 μg/mL), rGRN-2 is able to interact with unengaged PrLD within the mixture and drive its LSPS (Fig 7f, +25 RNA) similar to that observed in the absence of any RNA (Fig 7f, 0 RNA). In the condensates of PrLD-RNA generated with higher RNA concentrations (50-75 μg/mL), the external addition of rGRN-2 leads to minimal or no LSPS with the sustenance of RNA-PrLD condensates, as seen in the micrographs (Fig 7f, +50 and +75 RNA). This result reiterates the dominance of PrLD-RNA interactions over PrLD-GRN-2/rGRN-2 interactions and further supports the idea of displacement of GRN-2 from SGs in cells by RNA.

DISCUSSION

The precise role of GRNs in the pathophysiology of neurodegenerative disorders has remained an open question. In general, under what conditions and cellular cues are they generated from their percussor PGRN, and what role do they play in cellular functions and dysfunction has been a point of debate (Bateman, Belcourt, Bennett, Lazure, & Solomon, 1990; Bateman & Bennett, 1998; Holler et al., 2017; Horinokita et al., 2019; Kao, McKay, Singh, Brunet, & Huang, 2017; Root et al., 2021). What we do know is that PGRN secreted from microglia and astrocytes are transported into neuronal lysosomes by a sortilin-mediated pathway (Hu et al., 2010; Kao et al., 2017) and that the proteolytic processing generates GRNs within the lysosomes (Holler et al., 2017; Chris W. Lee et al., 2017) but what functional roles they play in lysosomes remain uncertain. PGRN also undergoes proteolytic cleavage extracellularly during inflammation (Zhu et al., 2002), and the fate of extracellular GRNs on neuronal functions also remains completely unknown. Here we investigated the cellular localization and interaction of extracellular GRNs (GRN-2, -3 and -5) with TDP-43 by treating them onto SHSY5Y neuroblastoma cells that transiently express TDP-43 PrLD. These studies along with in vitro biophysical investigations on the interactions between the two proteins in greater detail have brought out some unexpected properties of GRNs and PrLD that unravel GRNs' potential role in FTLD and related pathologies.

To understand the fate of extracellular GRNs on neurons, we labeled GRNs only with organic fluorophores (HiLyte) to visualize their uptake but were devoid of any tags that may predispose them for specific cellular localization. The data indicate that the GRNs are taken up by SH-SY5Y cells to be localized not only within lysosomes, which is well-known, but in the cytosol also. More importantly, GRNs colocalize with TDP-43 PrLD in the cytoplasm both under stress and non-stress conditions

indicating their potential involvement in FTLD and ALS pathologies (Fig 1). Furthermore, under stress conditions, based on the lack of FRAP recovery and absence of colocalization with the SG marker TIA1 (Fig S1), we could conclude that GRNs fail to partition within the SGs. In addition, we infer that the cytosolic colocalizations observed are complex cytoplasmic coacervates of PrLD and GRNs. Interestingly, unlike with PrLD, GRNs failed to colocalize with full-length TDP-43 either in non-stress conditions or within SGs under stress conditions (Fig S2), illustrating that GRNs may specifically interact with the pathogenic proteolytic fragments of TDP-43, for which the PrLD constitutes the major part (Feneberg et al., 2020), further implicating their role in pathology.

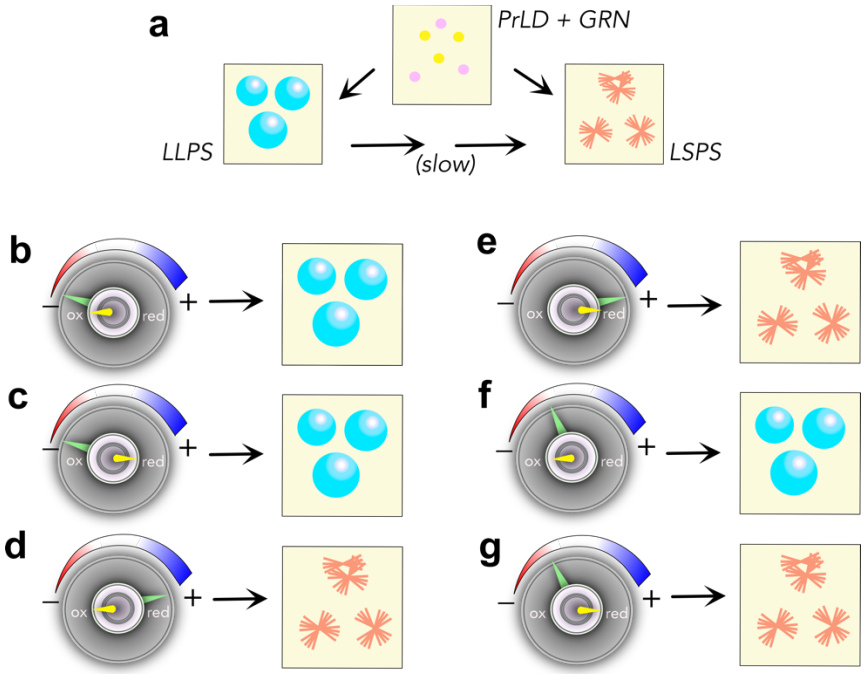

Figure 8. Schematic summary of complex coacervation between GRNs and PrLD. (a) Phase transitions of PrLD induced by GRNs. (b-g) Phase changes are coarsely controlled by electrostatic interactions (large knob) while they are finely controlled by the redox state (smaller knob) for some select conditions discovered in this report.

The dynamics of interactions between GRN-2 and PrLD investigated here have furthered our understanding of the possible mechanisms by which GRNs could modulate intracellular inclusions of TDP-43. Complex coacervation of TDP-43 with RNA has been known to be an electrostatically driven process (Babinchak et al., 2020; Lim et al., 2016). In a similar vein, we showed that coacervation with GRNs is likely driven by net charges on the protein (Bhopatkar et al., 2020). The charge distribution on GRNs 2, 3 and 5 shows that they are isoelectronic to negative charges, but with respect to positive charges, GRN-2 with +2 is in the middle between GRNs 3 and 5 (+4 and 0, respectively) (Fig 2). This facilitated the investigations on GRN-2's interactions with PrLD to draw biophysically meaningful inferences as GRN-3 and -5 have been shown to display a spectrum of phase transitions upon interacting with PrLD (Bhopatkar et al., 2020). The results presented here establish that the negative charges are the main driving forces of LLPS between GRNs and PrLD while the increase in the number of positive charges shifts the equilibrium towards LSPS (Fig 8a). To a lesser degree, hydrophobic interactions also seem to contribute possibly via cation - π and π - π interactions but certainly do not seem to drive LLPS.

Interestingly, by simply modulating the charges on GRNs, one could seemingly control the dynamics of phase transitions and complex coacervation with PrLD as summarized in Figure 8b-g. When under the control of purely negative charges on GRN, PrLD undergoes LLPS to form droplets that are demixed from the solution (Fig 8b and c). This can be explained based on polyphasic linkage and ligand binding effect on phase transitions as recently postulated by Ruff and coworkers (Ruff, Dar, & Pappu, 2021). Based on their work, preferential binding of a ligand (GRN) to the scaffold (PrLD) in dilute or dense phase can be expressed as;

$$C_{dil,L} = C_{dil}\left(\frac{P_{dil}}{P_{den}}\right)$$

Where $C_{dil,L}$ is concentration of the scaffold in the coexisting dilute phase in ligand's presence, P_{dil} and P_{den} are binding polynomials that define ligand binding to the scaffold in respective phases. If $P_{dil} > P_{den}$, i.e., binding of ligand to the scaffold is greater in the dilute phase, $C_{dil,L} > C_{den}$, LLPS gets suppressed and when $P_{dil} < P_{den}$ LLPS is augmented. Therefore, negative charges potentiate multivalent electrostatic charges with PrLD to preferentially partition into the dense phase, thus promoting LLPS. Increasing the number of positive charges to four shifts the equilibrium towards the formation of solid aggregates possibly by engaging in additional salt-bridge interactions with acidic residues of PrLD, preferably in the dilute phase (Fig 8d and e). These interactions, we speculate also promote aggregation. Unfortunately, we do not have experimental evidence for this extreme case (high positive charges and no negative charges), as such a mutant posed difficulties in recombinant expression (data not shown). However, the results obtained from GRN-7 (Fig S5), which has a high number of positive charge (+8) serves as a good proxy and strengthen the validity of the idea that GRNs have modulatory capabilities especially when it is known that not all GRNs level are the same in cells (T. Zhang et al., 2021).

Perhaps the most interesting aspect of this behavior is the role of cysteines and redox control. Our data indicate that when under compensatory positive and negative charge regimes in GRNs, redox conditions dictate the phase transitions (Fig 8f and g). Under fully reducing conditions, thiols in cysteines may participate in a network of hydrogen bonding interactions with Ser and/or Asn residues that are abundant in PrLD. Both these residues are conducive partners of cysteines as H-bonding donors and acceptors (Mazmanian, Sargsyan, Grauffel, Dudev, & Lim, 2016) and are abundant in PrLD (together accounting for ~40% of the sequence). Empirically, it is evident that these additional valences increase solute-solute interactions that shift the equilibrium out of the liquid-like state towards an aggregated state. The possibility of such a scenario is supported by the behavior of the alkylated forms of GRN-2 (Fig 5), where the polar acetamide adducts are capable of engaging in similar interactions. But under oxidizing conditions, the disulfide bonded cysteines preclude such interactions are abrogated, and therefore maintain weak and transient interactions that promote LLPS and a demixed state. From this, we surmise that the positively charged residues and thiols help fine-tune the phase transitions. It is also noteworthy that not an abrupt, but a continuum of phase changes is observed when traversing between one end of the redox spectrum to the other (Fig 5), which indicates that even under partially reducing conditions, LLPS can occur to some degree. Therefore, it seems plausible that GRN-PrLD droplets and aggregates could co-exist in the cytoplasm which largely presents a reducing environment.

The data presented here unambiguously establishes complex coacervation between PrLD and GRNs, yet, the absence of GRNs in SGs within PrLD or full-length TDP-43 expressing neuroblastoma cells seems to counter-intuitive at the outset. However, as observed by the ternary interactions between PrLD, GRN-2 and RNA, the reason for the inability of GRNs to partition into SGs is clear. GRN within the condensates of PrLD simply gets displaced by a stronger electrostatic ligand, RNA, which abrogates the

possibility of the three co-existing within the SGs. Given that SGs also contain many other phase separating proteins such as TIA1 (Kedersha et al., 2000), G3BP1 (Yang et al., 2020), hnRNPA1 (Guil, Long, & Cáceres, 2006) etc., the likelihood of GRNs partitioning into SGs is low. Furthermore, it is also interesting to observe that RNA is able to out-compete GRN-2 in reducing conditions where it forms insoluble aggregates with PrLD (Fig 7). This, along with the observed colocalization of GRN and PrLD in non-stress conditions, suggest that SGs mitigate potential toxicity posed by GRN-PrLD inclusions which eventually transition to amyloids, with an intervening gelated phase.

This report brings out the first evidence for the cellular uptake of extracellular GRNs and their cytoplasmic colocalization with PrLD. The exquisite control and tuning of complex coacervation of PrLD by GRNs via electrostatics and redox flux present intriguing possibilities by which GRNs can influence pathology. During acute inflammation, when GRNs are known to be generated in abundance by microglia and astrocytes (Ahmed, Mackenzie, Hutton, & Dickson, 2007; Baker & Manuelidis, 2003; Malaspina, Kaushik, & de Belleroche, 2001; Zhu et al., 2002), these pro-inflammatory molecules are taken up by neurons where they modulate the dynamics of cytotoxic proteolytic fragments of TDP-43. Even with haploinsufficiency of PGRN, which is a risk factor for FTLD, it can be conjectured that inflammation could lead to augmented production of GRNs that could compensate for the loss in PGRN (Zhu et al., 2002). Nevertheless, precisely what cellular consequences do these inclusions and coacervates possess remain unclear at this time. A few possibilities include mitochondrial, lysosomal, and autophagic dysfunction. Some of these will be unearthed in the coming years with the establishment of complex interactions and phase transitions between GRNs and TDP-43 PrLD as described in this report.

Materials and Methods

Recombinant expression and purification of proteins.

GRNs. GRNs (GRN-2, GRN-2(+/-), GRN-2(C/A), GRN-3, and GRN-5) were recombinantly expressed and purified as previously described, where GRN-3 was expressed in *Escherichia coli* SHuffle cells (New England Biolabs) while other GRNs were expressed in Origami 2 DE3 cells (Invitrogen) (Bhopatkar et al., 2020). Briefly, GRNs were expressed as fusion constructs containing an N-terminal thioredoxin-A, and His_6 tag with an intervening thrombin cleavage site. The fusion constructs were purified using immobilized-nickel affinity chromatography. The purified construct was cleaved using restriction grade bovine thrombin (BioPharm Laboratories) at 3 units/1 mg of protein for 24 h at room temperature to separate the fused tags. The sample was fractionated using semipreparative Jupiter 5 µm-10 x 250 mm C18 reverse-phase HPLC column (Phenomenex) using a gradient elution of 60%–80% acetonitrile containing 0.1% TFA. Fractionated protein was lyophilized and stored at -20°C. For the generation of 2-alkylated GRN-2 i.e. GRN-2 with two-free thiols that are alkylated, the protein was incubated with 10 molar excess of iodoacetamide post-thrombin cleavage for a period of 24 h at room temperature. Protein was then fractionated using reverse-phase HPLC as before. For the generation of 12-alkylated GRN-2 i.e. GRN-2 with all twelve thiols alkylated, the protein was incubated with 12x molar excess of TCEP post-thrombin cleavage for a period of 12 h at room temperature followed by incubation with 10 molar excess of iodoacetamide for 24 h at room temperature. Protein was then fractionated using reverse-phase HPLC as before. The purity of protein was confirmed using matrix assisted laser desorption-ionization time-of-flight mass spectroscopy (MALDI-ToF MS)

TDP-43 PrLD. PrLD was expressed and purified as described previously (Bhopatkar et al., 2020). The plasmid for TDP-43 PrLD was a gift from Dr. Nicolas Fawzi at Brown University (Addgene plasmid 98669, RRID: Addgene 98669). Briefly, the protein was expressed as a fusion construct with an N-

668 terminal His_6 tag followed by tobacco etch virus (TEV) protease cleavage site in *E.coli* BL21 DE3 Star
669 cells (Invitrogen). The fusion construct was purified using immobilized-nickel affinity chromatography.
670 Purified protein was concentrated using Amicon Ultra-Centrifugal units (Millipore) and flash frozen for
671 storage at -80°C or used immediately for experiments.

672 **Preparation of proteins and RNA**

673 ***GRNs.*** Lyophilized protein was resuspended in required buffer **(**20 mM MES, pH 6.0 or 20 mM
674 ammonium formate, pH 4.5) and the concentration was estimated spectrophotometrically at 280 nm with
675 extinction coefficients of 6250 M^{-1} cm^{-1} for GRN-2, GRN-2(+/-) and GRN-3, 5500 M^{-1} cm^{-1} for GRN-
676 2(C/A), 7740 M^{-1} cm^{-1} for GRN-5 at 280 nm. The number of free thiols within GRNs was estimated using
677 Ellman's assay and by alkylation with iodoacetamide, as described previously(Ghag et al., 2017). The
678 reduced forms of GRNs were generated by incubating the freshly purified proteins with 12x molar excess
679 of tris(2-carboxyethyl)phosphine (TCEP) at room temperature for 2-4 h or at 4°C for ~12 h. Fluorescent
680 labeling of GRNs was performed using HiLyte™ Fluor 405 succinimidyl ester (Anaspec) or HiLyte™
681 Fluor 647 succinimidyl ester for FRAP studies on GRNs. Proteins were incubated with 3 molar excess of
682 dyes at 4°C for ~12 h and excess dye was excluded using clarion MINI Spin Columns, Desalt S-25
683 (Sorbent Technologies Inc).

684 ***PrLD***. Before the experiments, the protein was buffer-exchanged into 20 mM MES, pH 6.0 or 20 mM
685 ammonium formate, pH 4.5, using PD SpinTrap G-25 desalting columns (Cytiva) and the concentration
686 was estimated using an extinction coefficient of 19480 M^{-1} cm^{-1} at 280 nm. Fluorescent labeling of PrLD
687 was performed using HiLyte™ Fluor 647 succinimidyl ester (Anaspec) using a similar protocol as
688 described above for GRNs.

689 ***RNA.*** Lyophilized poly-A (Sigma Aldrich) was resuspended in deionized, sterilized water at a
690 concentration of 1 mg/mL. The concentration of the stock was estimated by considering a value of 1
691 absorbance unit to correspond to 40 μg of RNA. The prepared stock was flash frozen and stored at -80°C.
692 Aliquots of prepared stock were thawed and used immediately for experiments.

693

694 **Cell growth, transfection and colocalization analysis**

695 SH-SY5Y neuroblastoma cells (ATCC, Manassas, VA) were grown in DMEM:F12 (1:1) media
696 containing 10% FBS (Gibco, Thermo Scientific) and were maintained in humidified condition at 37 °C
697 with 5.5% CO_2. Cells were seeded 24 hours before transfection. Cells were transfected with PrLD-
698 SBFP2 or wtTDP43tdTomato plasmid using the TransIT-X2® dynamic delivery system, Mirius (1:3) in
699 Opti-MEM media (Thermo scientific). Cell confluency was allowed to reach 70-80% prior to
700 transfection. After 24 h, cells were gently washed for two times with fresh media and 500 nM of
701 fluorescently labeled recombinant GRNs were added. Cells were incubated with GRN-containing media
702 for 24 hours. Following this, media was replaced with GRN-devoid media and cells were incubated for a
703 further 1 h. For inducing stress, sodium arsenite was added at a final concentration of 0.5 mM and
704 incubated for 30 minutes. Cells were stained with nuclear (NucSpot® Live 650, Biotium) or lysosomal
705 (Lysoview™ 650, Biotium) markers prior to imaging at 40X magnification using Leica STELLARIS-
706 DMI8 microscope. For colocalization analysis of GRNs and PrLD, the respective channels for PrLD and
707 GRNs were converted to 16-bit grayscale format and region of interest was selected. Images were
708 processed using Coloc2 parameter in FIJI imageJ software using Costes threshold regression, and
709 Manders' tM1 values were reported. All the confocal images were processed using Adobe illustrator and
710 data were processed using OriginPro 8.5 software.

711

712

713 **Immunofluorescence**

714 For immunofluorescence experiment, cells were plated in a 12 well plate 24 h prior to transfection with
715 PrLD-SBFP2 as described above. After incubating with fluorophore labeled-GRNs for 24 h, media was
716 replaced, and experiments were carried out in both stress and non-stress conditions. For induction of
717 stress, 0.5 mM sodium arsenite was added to the media and incubated for 30 minutes followed by
718 washing with 1x PBS. Cells were fixed in 4% paraformaldehyde for 20 minutes and washed twice with
719 1x PBS. These were further permeabilized with 0.2% Triton X-100 in 1x PBS for 20 minutes. Cells were
720 washed and blocked using 3% BSA for 2 h. Cells were incubated with anti-TIA1 primary antibodies (Cell
721 Signaling Technology, TIAR XP® Rabbit mAb #8509) and anti-rabbit secondary antibodies (Cell
722 Signaling Technology, Alexa Flour® 488 conjugate #4412) and imaged following the addition of anti-
723 fade mounting media at 40X magnification on Leica STELLARIS-DMI8 microscope.

724 **DIC Microscopy and FRAP analysis**

725 DIC and fluorescence microscopy images were acquired on Leica STELLARIS-DMI8 microscope. The
726 assays were performed in an optical bottom 96 well-plate (Thermo) and were covered with an optically
727 clear sealing tape (Nunc, Thermo Scientific) to prevent evaporation. The reactions were initiated at room
728 temperature and were visualized within 10-15 mins of mixing. Brightfield and fluorescence images were
729 acquired at a magnification of 40x or 63x with an oil immersion objective. For microscopically
730 monitoring the ternary interactions between GRN-2, PrLD and RNA; we initially generated heterotypic
731 condensates of GRN-2 and PrLD, followed by titration with desired volumes of the RNA stock. Images
732 were acquired after an equilibration time of ~10-15 mins after each titration. The RNA stocks were
733 prepared at a high initial concentration to minimize dilution effects upon titration. For fluorescence
734 imaging and FRAP studies, samples were prepared by mixing the required concentration of proteins in an
735 optical-bottom 96 well plate in the presence of 1% fluorophore labelled proteins. For FRAP studies,
736 fluorescence intensities were acquired pre- (~2 seconds) and post-bleach (~30 seconds) at an interval of
737 68 μs. Bleaching period was varied from 10-20 seconds with a laser intensity of 100% while the laser
738 intensity for imaging was set at 2-10%. The fluorescence recovery data was processed using Leica LasX
739 program and Origin 8.5 graphing software. The recovery curves of individual samples were normalized
740 with respect to the pre-bleach fluorescence intensities. To discern the rate constants of recovery kinetics
741 post-bleach the initial-rate method was utilized (Buell et al., 2014; Dean, Rana, Campbell, Ghosh, &
742 Rangachari, 2018). Briefly, period of fluorescence recovery 1 second post-bleach was evaluated via a
743 linear fit with the slope of the line providing a rate constant, k (s^{-1}). Rate constants were obtained by
744 evaluating three FRAP recovery curves for each sample. For time-course experiments, FRAP analysis
745 was performed on samples at initial time (0 h) and after incubation of 24 h at 37°C under quiescent
746 conditions. A noteworthy point is that we observed significant photobleaching of HiLyte-405 when
747 performing FRAP analysis of GRNs labeled with the fluorophore precluding the use of this dye in this
748 study. To obtain this data, we then cross-labeled GRNs with HiLyte-647 (for performing FRAP studies)
749 and PrLD with HiLyte-405 (only for visualization).

750 **Post imaging analysis**

751 ***Droplet area distribution***. Area of the droplets formed within various samples was ascertained using the
752 ImageJ program. Briefly, the fluorescence images acquired for the respective samples were subjected to
753 color thresholding at default values in the program. Area of droplets within the threshold images were
754 then extracted using the included particle analyzer tool of the program. A lower limit of either 50 or 200
755 ($pixel^2$) (depending on image magnification) was placed on area of particles to be analyzed so as to
756 exclude detection of small artifacts. Areas obtained in $pixel^2$ were converted into μm^2 by considering the

757 scale-bar. The obtained data was then plot as a histogram overlayed with normal distribution curve using
758 Origin 8.5. A set of 100 droplets were enumerated from at least two different fields for each sample
759 ***Fluorescence intensity profiles***. To qualitatively ascertain the displacement of GRN-2 from condensates
760 upon titration with RNA, we determined the fluorescence intensity profiles of the fluorophore labeled
761 proteins from the images of the respective samples using the ImageJ program. Intensity profiles were
762 obtained by mapping a line segment across the width of a droplet and extracting the intensities of the
763 fluorophores (HiLyte 405 for GRN-2 and HiLyte 647 for PrLD) using the plot-profile tool. The plot-
764 profile tool provides intensity values within an arbitrary window of 0-80 units, with highly fluorescent
765 samples being cut-off at the upper limit. The fluorophore intensities obtained in a pixel scale were then
766 converted into μm using the scale-bar. The fluorescence intensity profile was extracted from individual
767 droplets for each sample but are representative of the entire field.
768
769 **Turbidimetric assays**
770 Turbidity measurements were performed on a BioTek Synergy H1 microplate reader. Reactions were
771 initiated and allowed to equilibrate at room temperature for 5-10 mins before each measurement. For
772 titration experiments with GRNs, NaCl, or RNA, stocks were prepared at high concentrations to minimize
773 dilution of samples. For establishment of phase diagrams, a boundary value of 0.140 OD_{600} was set and
774 readings above it were considered to undergo phase transition. Temperature dependent phase diagram was
775 established by equilibrating samples at respective temperature (4°C, room temperature) for 15 mins, while
776 temperatures above 30°C were achieved using the internal temperature control capability of the plate
777 reader. Data processing was performed on Origin 8.5.
778
779 **Aggregation assay**
780 To monitor the amyloid-formation of PrLD in presence of GRN-2 or rGRN-2, thioflavin-T (ThT)
781 fluorescence assays were performed on BioTek Synergy H1 microplate reader. The aggregation of PrLD
782 was monitored in the presence of different molar concentrations of GRN-2 or rGRN-2 in separate
783 reactions in the presence of 15 μM ThT dye. The reactions were monitored for a period of 24 h under
784 quiescent conditions at 37°C.
785
786 **MALDI-ToF MS**
787 For confirming the purity and for characterization of proteins used, MALDI-ToF MS spectroscopy was
788 performed on a Bruker Daltonics Microflex LT/SH TOF-MS system. Prepared samples were spotted onto
789 a Bruker MSP 96 MicroScout Target microchip with a 1:1 ratio of sample:sinapinic acid matrix in
790 saturated acetonitrile and water. Instrument calibration was performed using Bruker Protein Calibration
791 Standard I (Bruker Daltonics). Alkylation assays of GRNs using iodoacetamide were performed as
792 described (Bhopatkar & Rangachari, 2021).
793
794 **In-silico analysis and figure preparation**
795 Redox-dependent disorder scores for individual proteins were obtained using IUPred2A platform(Erdős
796 & Dosztányi, 2020). Specifically, the FASTA sequence of each protein was evaluated by coupling the
797 IUPred2 long disorder algorithm with a Redox-state tool (Mészáros et al., 2018). The obtained figures
798 were processed using the Adobe Illustrator CC suite and Affinity Designer®.
799
800

Acknowledgements

The authors would like to thank the following agencies for financial support: National Institute of Aging (1R56AG062292-01) and the National Science Foundation (NSF CBET 1802793) to VR. The authors also thank the National Center for Research Resources (5P20RR01647-11) and the National Institute of General Medical Sciences (8 P20 GM103476-11) from the National Institutes of Health for funding through INBRE for the use of their core facilities.

Competing interests statement

The authors declare that they have no financial or non-financial interests.

References

Ahmed, Z., Mackenzie, I. R., Hutton, M. L., & Dickson, D. W. (2007). Progranulin in frontotemporal lobar degeneration and neuroinflammation. *J Neuroinflammation, 4*, 7. doi:10.1186/1742-2094-4-7

Arrant, A. E., Onyilo, V. C., Unger, D. E., & Roberson, E. D. (2018). Progranulin Gene Therapy Improves Lysosomal Dysfunction and Microglial Pathology Associated with Frontotemporal Dementia and Neuronal Ceroid Lipofuscinosis. *The Journal of Neuroscience, 38*(9), 2341. doi:10.1523/JNEUROSCI.3081-17.2018

Babinchak, W. M., Dumm, B. K., Venus, S., Boyko, S., Putnam, A. A., Jankowsky, E., & Surewicz, W. K. (2020). Small molecules as potent biphasic modulators of protein liquid-liquid phase separation. *Nature Communications, 11*(1), 5574. doi:10.1038/s41467-020-19211-z

Baker, C. A., & Manuelidis, L. (2003). Unique inflammatory RNA profiles of microglia in Creutzfeldt-Jakob disease. *Proc Natl Acad Sci U S A, 100*(2), 675-679. doi:10.1073/pnas.0237313100

Bang, J., Spina, S., & Miller, B. L. (2015). Frontotemporal dementia. *Lancet, 386*(10004), 1672-1682. doi:10.1016/s0140-6736(15)00461-4

Bateman, A., Belcourt, D., Bennett, H., Lazure, C., & Solomon, S. (1990). Granulins, a novel class of peptide from leukocytes. *Biochem Biophys Res Commun, 173*(3), 1161-1168. doi:10.1016/s0006-291x(05)80908-8

Bateman, A., & Bennett, H. P. (1998). Granulins: the structure and function of an emerging family of growth factors. *J Endocrinol, 158*(2), 145-151. doi:10.1677/joe.0.1580145

Bhopatkar, A. A., & Rangachari, V. (2021). Are granulins copper sequestering proteins? *Proteins, 89*(4), 450-461. doi:10.1002/prot.26031

Bhopatkar, A. A., Uversky, V. N., & Rangachari, V. (2020). Granulins modulate liquid-liquid phase separation and aggregation of the prion-like C-terminal domain of the neurodegeneration-associated protein TDP-43. *The Journal of biological chemistry, 295*(8), 2506-2519. doi:10.1074/jbc.RA119.011501

Brangwynne, Clifford P., Tompa, P., & Pappu, Rohit V. (2015). Polymer physics of intracellular phase transitions. *Nature Physics, 11*(11), 899-904. doi:10.1038/nphys3532

Buell, A. K., Galvagnion, C., Gaspar, R., Sparr, E., Vendruscolo, M., Knowles, T. P., . . . Dobson, C. M. (2014). Solution conditions determine the relative importance of nucleation and growth processes in α-synuclein aggregation. *Proc Natl Acad Sci U S A, 111*(21), 7671-7676. doi:10.1073/pnas.1315346111

Buratti, E., & Baralle, F. E. (2008). Multiple roles of TDP-43 in gene expression, splicing regulation, and human disease. *Front Biosci, 13*, 867-878. doi:10.2741/2727

Buratti, E., Dörk, T., Zuccato, E., Pagani, F., Romano, M., & Baralle, F. E. (2001). Nuclear factor TDP-43 and SR proteins promote in vitro and in vivo CFTR exon 9 skipping. *Embo j, 20*(7), 1774-1784. doi:10.1093/emboj/20.7.1774

Chitramuthu, B. P., Bennett, H. P. J., & Bateman, A. (2017). Progranulin: a new avenue towards the understanding and treatment of neurodegenerative disease. *Brain, 140*(12), 3081-3104. doi:10.1093/brain/awx198

Choi, J.-M., Dar, F., & Pappu, R. V. (2019). LASSI: A lattice model for simulating phase transitions of multivalent proteins. *PLOS Computational Biology, 15*(10), e1007028. doi:10.1371/journal.pcbi.1007028

Choi, J.-M., Holehouse, A. S., & Pappu, R. V. (2020). Physical Principles Underlying the Complex Biology of Intracellular Phase Transitions. *Annual Review of Biophysics, 49*(1), 107-133. doi:10.1146/annurev-biophys-121219-081629

Chow, T. W., Miller, B. L., Hayashi, V. N., & Geschwind, D. H. (1999). Inheritance of Frontotemporal Dementia. *Archives of Neurology, 56*(7), 817-822. doi:10.1001/archneur.56.7.817

Ciryam, P., Lambert-Smith, I. A., Bean, D. M., Freer, R., Cid, F., Tartaglia, G. G., . . . Yerbury, J. J. (2017). Spinal motor neuron protein supersaturation patterns are associated with inclusion body formation in ALS. *Proceedings of the National Academy of Sciences, 114*(20), E3935. doi:10.1073/pnas.1613854114

Colombrita, C., Zennaro, E., Fallini, C., Weber, M., Sommacal, A., Buratti, E., . . . Ratti, A. (2009). TDP-43 is recruited to stress granules in conditions of oxidative insult. *Journal of Neurochemistry, 111*(4), 1051-1061. doi:https://doi.org/10.1111/j.1471-4159.2009.06383.x

Conicella, A. E., Zerze, G. H., Mittal, J., & Fawzi, N. L. (2016). ALS Mutations Disrupt Phase Separation Mediated by α-Helical Structure in the TDP-43 Low-Complexity C-Terminal Domain. *Structure, 24*(9), 1537-1549. doi:10.1016/j.str.2016.07.007

Correia, A. S., Patel, P., Dutta, K., & Julien, J.-P. (2015). Inflammation Induces TDP-43 Mislocalization and Aggregation. *PLOS ONE, 10*(10), e0140248-e0140248. doi:10.1371/journal.pone.0140248

Dean, D. N., Rana, P., Campbell, R. P., Ghosh, P., & Rangachari, V. (2018). Propagation of an Aβ Dodecamer Strain Involves a Three-Step Mechanism and a Key Intermediate. *Biophys J, 114*(3), 539-549. doi:10.1016/j.bpj.2017.11.3778

Düster, R., Kaltheuner, I. H., Schmitz, M., & Geyer, M. (2021). 1,6-Hexanediol, commonly used to dissolve liquid–liquid phase separated condensates, directly impairs kinase and phosphatase activities. *Journal of Biological Chemistry, 296*. doi:10.1016/j.jbc.2021.100260

Elia, L. P., Mason, A. R., Alijagic, A., & Finkbeiner, S. (2019). Genetic Regulation of Neuronal Progranulin Reveals a Critical Role for the Autophagy-Lysosome Pathway. *The Journal of Neuroscience, 39*(17), 3332. doi:10.1523/JNEUROSCI.3498-17.2019

Erdős, G., & Dosztányi, Z. (2020). Analyzing Protein Disorder with IUPred2A. *Current Protocols in Bioinformatics, 70*(1), e99. doi:https://doi.org/10.1002/cpbi.99

Fang, M. Y., Markmiller, S., Vu, A. Q., Javaherian, A., Dowdle, W. E., Jolivet, P., . . . Yeo, G. W. (2019). Small-Molecule Modulation of TDP-43 Recruitment to Stress Granules Prevents Persistent TDP-43 Accumulation in ALS/FTD. *Neuron, 103*(5), 802-819.e811. doi:10.1016/j.neuron.2019.05.048

Feneberg, E., Charles, P. D., Finelli, M. J., Scott, C., Kessler, B. M., Fischer, R., . . . Turner, M. R. (2020). Detection and quantification of novel C-terminal TDP-43 fragments in ALS-TDP. *Brain Pathol*, e12923. doi:10.1111/bpa.12923

François-Moutal, L., Perez-Miller, S., Scott, D. D., Miranda, V. G., Mollasalehi, N., & Khanna, M. (2019). Structural Insights Into TDP-43 and Effects of Post-translational Modifications. *Frontiers in Molecular Neuroscience, 12*(301). doi:10.3389/fnmol.2019.00301

Gao, X., Joselin, A. P., Wang, L., Kar, A., Ray, P., Bateman, A., . . . Wu, J. Y. (2010). Progranulin promotes neurite outgrowth and neuronal differentiation by regulating GSK-3β. *Protein Cell, 1*(6), 552-562. doi:10.1007/s13238-010-0067-1

Gass, J., Lee, W. C., Cook, C., Finch, N., Stetler, C., Jansen-West, K., . . . Petrucelli, L. (2012). Progranulin regulates neuronal outgrowth independent of sortilin. *Mol Neurodegener, 7*, 33. doi:10.1186/1750-1326-7-33

Gasset-Rosa, F., Lu, S., Yu, H., Chen, C., Melamed, Z., Guo, L., . . . Cleveland, D. W. (2019). Cytoplasmic TDP-43 De-mixing Independent of Stress Granules Drives Inhibition of Nuclear Import, Loss of Nuclear TDP-43, and Cell Death. *Neuron, 102*(2), 339-357.e337. doi:10.1016/j.neuron.2019.02.038

Ghag, G., Holler, C. J., Taylor, G., Kukar, T. L., Uversky, V. N., & Rangachari, V. (2017). Disulfide bonds and disorder in granulin-3: An unusual handshake between structural stability and plasticity. *Protein Science, 26*(9), 1759-1772. doi:https://doi.org/10.1002/pro.3212

Gilks, N., Kedersha, N., Ayodele, M., Shen, L., Stoecklin, G., Dember, L. M., & Anderson, P. (2004). Stress Granule Assembly Is Mediated by Prion-like Aggregation of TIA-1. *Molecular Biology of the Cell, 15*(12), 5383-5398. doi:10.1091/mbc.e04-08-0715

Grossman, M. (2002). Frontotemporal dementia: a review. *J Int Neuropsychol Soc, 8*(4), 566-583. doi:10.1017/s1355617702814357

Guil, S., Long, J. C., & Cáceres, J. F. (2006). hnRNP A1 relocalization to the stress granules reflects a role in the stress response. *Mol Cell Biol, 26*(15), 5744-5758. doi:10.1128/mcb.00224-06

He, Z., & Bateman, A. (1999). Progranulin Gene Expression Regulates Epithelial Cell Growth and Promotes Tumor Growth <em>in Vivo</em&gt. *Cancer Res, 59*(13), 3222.

He, Z., & Bateman, A. (2003). Progranulin (granulin-epithelin precursor, PC-cell-derived growth factor, acrogranin) mediates tissue repair and tumorigenesis. *J Mol Med, 81*(10), 600-612.

Herman Allison, B., Silva Afonso, M., Kelemen Sheri, E., Ray, M., Vrakas Christine, N., Burke Amy, C., . . . Autieri Michael, V. (2019). Regulation of Stress Granule Formation by Inflammation, Vascular Injury, and Atherosclerosis. *Arteriosclerosis, Thrombosis, and Vascular Biology, 39*(10), 2014-2027. doi:10.1161/ATVBAHA.119.313034

Holler, C. J., Taylor, G., Deng, Q., & Kukar, T. (2017). Intracellular Proteolysis of Progranulin Generates Stable, Lysosomal Granulins that Are Haploinsufficient in Patients with Frontotemporal Dementia Caused by GRN Mutations. *eNeuro, 4*(4). doi:10.1523/eneuro.0100-17.2017

Hoque, M., Mathews, M. B., & Pe'ery, T. (2010). Progranulin (granulin/epithelin precursor) and its constituent granulin repeats repress transcription from cellular promoters. *J Cell Physiol, 223*(1), 224-233. doi:10.1002/jcp.22031

Horinokita, I., Hayashi, H., Oteki, R., Mizumura, R., Yamaguchi, T., Usui, A., . . . Takagi, N. (2019). Involvement of Progranulin and Granulin Expression in Inflammatory Responses after Cerebral Ischemia. *Int J Mol Sci, 20*(20). doi:10.3390/ijms20205210

Hu, F., Padukkavidana, T., Vægter, C. B., Brady, O. A., Zheng, Y., Mackenzie, I. R., . . . Strittmatter, S. M. (2010). Sortilin-mediated endocytosis determines levels of the frontotemporal dementia protein, progranulin. *Neuron, 68*(4), 654-667. doi:10.1016/j.neuron.2010.09.034

Igaz, L. M., Kwong, L. K., Chen-Plotkin, A., Winton, M. J., Unger, T. L., Xu, Y., . . . Lee, V. M. Y. (2009). Expression of TDP-43 C-terminal Fragments in Vitro Recapitulates Pathological Features of TDP-43 Proteinopathies. *The Journal of biological chemistry, 284*(13), 8516-8524. doi:10.1074/jbc.M809462200

Igaz, L. M., Kwong, L. K., Xu, Y., Truax, A. C., Uryu, K., Neumann, M., . . . Lee, V. M. (2008). Enrichment of C-terminal fragments in TAR DNA-binding protein-43 cytoplasmic inclusions in brain but not in spinal cord of frontotemporal lobar degeneration and amyotrophic lateral sclerosis. *Am J Pathol, 173*(1), 182-194. doi:10.2353/ajpath.2008.080003

Irwin, D. J., Cairns, N. J., Grossman, M., McMillan, C. T., Lee, E. B., Van Deerlin, V. M., . . . Trojanowski, J. Q. (2015). Frontotemporal lobar degeneration: defining phenotypic diversity through personalized medicine. *Acta Neuropathologica, 129*(4), 469-491. doi:10.1007/s00401-014-1380-1

Jian, J., Konopka, J., & Liu, C. (2013). Insights into the role of progranulin in immunity, infection, and inflammation. *Journal of leukocyte biology, 93*(2), 199-208. doi:10.1189/jlb.0812429

Kao, A. W., McKay, A., Singh, P. P., Brunet, A., & Huang, E. J. (2017). Progranulin, lysosomal regulation and neurodegenerative disease. *Nat Rev Neurosci, 18*(6), 325-333. doi:10.1038/nrn.2017.36

Kaur, T., Raju, M., Alshareedah, I., Davis, R. B., Potoyan, D. A., & Banerjee, P. R. (2021). Sequence-encoded and composition-dependent protein-RNA interactions control multiphasic condensate morphologies. *Nature Communications, 12*(1), 872. doi:10.1038/s41467-021-21089-4

Kedersha, N., Cho, M. R., Li, W., Yacono, P. W., Chen, S., Gilks, N., . . . Anderson, P. (2000). Dynamic shuttling of TIA-1 accompanies the recruitment of mRNA to mammalian stress granules. *The Journal of cell biology, 151*(6), 1257-1268. doi:10.1083/jcb.151.6.1257

Khalfallah, Y., Kuta, R., Grasmuck, C., Prat, A., Durham, H. D., & Vande Velde, C. (2018). TDP-43 regulation of stress granule dynamics in neurodegenerative disease-relevant cell types. *Scientific Reports, 8*(1), 7551. doi:10.1038/s41598-018-25767-0

Lee, C. W., Stankowski, J. N., Chew, J., Cook, C. N., Lam, Y.-W., Almeida, S., . . . Petrucelli, L. (2017). The lysosomal protein cathepsin L is a progranulin protease. *Molecular Neurodegeneration, 12*(1), 55. doi:10.1186/s13024-017-0196-6

Lee, C. W., Stankowski, J. N., Chew, J., Cook, C. N., Lam, Y. W., Almeida, S., . . . Petrucelli, L. (2017). The lysosomal protein cathepsin L is a progranulin protease. *Mol Neurodegener, 12*(1), 55. doi:10.1186/s13024-017-0196-6

Li, H.-R., Chiang, W.-C., Chou, P.-C., Wang, W.-J., & Huang, J.-R. (2018). TAR DNA-binding protein 43 (TDP-43) liquid-liquid phase separation is mediated by just a few aromatic residues. *The Journal of biological chemistry, 293*(16), 6090-6098. doi:10.1074/jbc.AC117.001037

Li, H. R., Chen, T. C., Hsiao, C. L., Shi, L., Chou, C. Y., & Huang, J. R. (2018). The physical forces mediating self-association and phase-separation in the C-terminal domain of TDP-43. *Biochim Biophys Acta Proteins Proteom, 1866*(2), 214-223. doi:10.1016/j.bbapap.2017.10.001

Lim, L., Wei, Y., Lu, Y., & Song, J. (2016). ALS-Causing Mutations Significantly Perturb the Self-Assembly and Interaction with Nucleic Acid of the Intrinsically Disordered Prion-Like Domain of TDP-43. *PLoS Biol, 14*(1), e1002338. doi:10.1371/journal.pbio.1002338

Liu-Yesucevitz, L., Bilgutay, A., Zhang, Y.-J., Vanderwyde, T., Citro, A., Mehta, T., . . . Wolozin, B. (2010). Tar DNA Binding Protein-43 (TDP-43) Associates with Stress Granules: Analysis of Cultured Cells and Pathological Brain Tissue. *PLOS ONE, 5*(10), e13250. doi:10.1371/journal.pone.0013250

López-Mirabal, H. R., & Winther, J. R. (2008). Redox characteristics of the eukaryotic cytosol. *Biochimica et Biophysica Acta (BBA) - Molecular Cell Research, 1783*(4), 629-640. doi:https://doi.org/10.1016/j.bbamcr.2007.10.013

Mackenzie, I. R., Munoz, D. G., Kusaka, H., Yokota, O., Ishihara, K., Roeber, S., . . . Neumann, M. (2011). Distinct pathological subtypes of FTLD-FUS. *Acta Neuropathol, 121*(2), 207-218. doi:10.1007/s00401-010-0764-0

Mackenzie, I. R. A., & Rademakers, R. (2008). The role of transactive response DNA-binding protein-43 in amyotrophic lateral sclerosis and frontotemporal dementia. *Current opinion in neurology, 21*(6), 693-700. doi:10.1097/WCO.0b013e3283168d1d

Majumdar, A., Dogra, P., Maity, S., & Mukhopadhyay, S. (2019). Liquid–Liquid Phase Separation Is Driven by Large-Scale Conformational Unwinding and Fluctuations of Intrinsically Disordered Protein Molecules. *The Journal of Physical Chemistry Letters, 10*(14), 3929-3936. doi:10.1021/acs.jpclett.9b01731

Malaspina, A., Kaushik, N., & de Belleroche, J. (2001). Differential expression of 14 genes in amyotrophic lateral sclerosis spinal cord detected using gridded cDNA arrays. *J Neurochem, 77*(1), 132-145. doi:10.1046/j.1471-4159.2001.t01-1-00231.x

Mao, Q., Wang, D., Li, Y., Kohler, M., Wilson, J., Parton, Z., . . . Bigio, E. H. (2017). Disease and Region Specificity of Granulin Immunopositivities in Alzheimer Disease and Frontotemporal

Lobar Degeneration. *Journal of Neuropathology & Experimental Neurology, 76*(11), 957-968. doi:10.1093/jnen/nlx085

Mazmanian, K., Sargsyan, K., Grauffel, C., Dudev, T., & Lim, C. (2016). Preferred Hydrogen-Bonding Partners of Cysteine: Implications for Regulating Cys Functions. *The Journal of Physical Chemistry B, 120*(39), 10288-10296. doi:10.1021/acs.jpcb.6b08109

Mészáros, B., Erdos, G., & Dosztányi, Z. (2018). IUPred2A: context-dependent prediction of protein disorder as a function of redox state and protein binding. *Nucleic Acids Res, 46*(W1), W329-w337. doi:10.1093/nar/gky384

Muiznieks, L. D., Sharpe, S., Pomès, R., & Keeley, F. W. (2018). Role of Liquid–Liquid Phase Separation in Assembly of Elastin and Other Extracellular Matrix Proteins. *Journal of Molecular Biology, 430*(23), 4741-4753. doi:https://doi.org/10.1016/j.jmb.2018.06.010

Neumann, M., Sampathu, D. M., Kwong, L. K., Truax, A. C., Micsenyi, M. C., Chou, T. T., . . . Lee, V. M. (2006). Ubiquitinated TDP-43 in frontotemporal lobar degeneration and amyotrophic lateral sclerosis. *Science, 314*(5796), 130-133. doi:10.1126/science.1134108

Nunes, C., Mestre, I., Marcelo, A., Koppenol, R., Matos, C. A., & Nóbrega, C. (2019). MSGP: the first database of the protein components of the mammalian stress granules. *Database, 2019*. doi:10.1093/database/baz031

Pak, C. W., Kosno, M., Holehouse, A. S., Padrick, S. B., Mittal, A., Ali, R., . . . Rosen, M. K. (2016). Sequence Determinants of Intracellular Phase Separation by Complex Coacervation of a Disordered Protein. *Mol Cell, 63*(1), 72-85. doi:10.1016/j.molcel.2016.05.042

Park, B., Buti, L., Lee, S., Matsuwaki, T., Spooner, E., Brinkmann, M. M., . . . Ploegh, H. L. (2011). Granulin is a soluble cofactor for toll-like receptor 9 signaling. *Immunity, 34*(4), 505-513. doi:10.1016/j.immuni.2011.01.018

Plowman, G. D., Green, J. M., Neubauer, M. G., Buckley, S. D., McDonald, V. L., Todaro, G. J., & Shoyab, M. (1992). The epithelin precursor encodes two proteins with opposing activities on epithelial cell growth. *The Journal of biological chemistry, 267*(18), 13073-13078.

Prasad, A., Bharathi, V., Sivalingam, V., Girdhar, A., & Patel, B. K. (2019). Molecular Mechanisms of TDP-43 Misfolding and Pathology in Amyotrophic Lateral Sclerosis. *Frontiers in Molecular Neuroscience, 12*(25). doi:10.3389/fnmol.2019.00025

Protter, D. S. W., & Parker, R. (2016). Principles and Properties of Stress Granules. *Trends in cell biology, 26*(9), 668-679. doi:10.1016/j.tcb.2016.05.004

Root, J., Merino, P., Nuckols, A., Johnson, M., & Kukar, T. (2021). Lysosome dysfunction as a cause of neurodegenerative diseases: Lessons from frontotemporal dementia and amyotrophic lateral sclerosis. *Neurobiology of Disease, 154*, 105360. doi:https://doi.org/10.1016/j.nbd.2021.105360

Ruff, K. M., Dar, F., & Pappu, R. V. (2021). Ligand effects on phase separation of multivalent macromolecules. *Proceedings of the National Academy of Sciences, 118*(10), e2017184118. doi:10.1073/pnas.2017184118

Ryan, C. L., Baranowski, D. C., Chitramuthu, B. P., Malik, S., Li, Z., Cao, M., . . . Bateman, A. (2009). Progranulin is expressed within motor neurons and promotes neuronal cell survival. *BMC Neurosci, 10*, 130. doi:10.1186/1471-2202-10-130

Salazar, D. A., Butler, V. J., Argouarch, A. R., Hsu, T.-Y., Mason, A., Nakamura, A., . . . Kao, A. W. (2015). The Progranulin Cleavage Products, Granulins, Exacerbate TDP-43 Toxicity and Increase TDP-43 Levels. *The Journal of Neuroscience, 35*(25), 9315. doi:10.1523/JNEUROSCI.4808-14.2015

Sama, R. R. K., Ward, C. L., Kaushansky, L. J., Lemay, N., Ishigaki, S., Urano, F., & Bosco, D. A. (2013). FUS/TLS assembles into stress granules and is a prosurvival factor during hyperosmolar stress. *J Cell Physiol, 228*(11), 2222-2231. doi:10.1002/jcp.24395

Seelaar, H., Rohrer, J. D., Pijnenburg, Y. A., Fox, N. C., & van Swieten, J. C. (2011). Clinical, genetic and pathological heterogeneity of frontotemporal dementia: a review. *J Neurol Neurosurg Psychiatry, 82*(5), 476-486. doi:10.1136/jnnp.2010.212225

Shoyab, M., McDonald, V. L., Byles, C., Todaro, G. J., & Plowman, G. D. (1990). Epithelins 1 and 2: isolation and characterization of two cysteine-rich growth-modulating proteins. *Proc Natl Acad Sci U S A, 87*(20), 7912-7916. doi:10.1073/pnas.87.20.7912

Shulga, N., & Goldfarb, D. S. (2003). Binding dynamics of structural nucleoporins govern nuclear pore complex permeability and may mediate channel gating. *Mol Cell Biol, 23*(2), 534-542. doi:10.1128/mcb.23.2.534-542.2003

Sun, Y., & Chakrabartty, A. (2017). Phase to Phase with TDP-43. *Biochemistry, 56*(6), 809-823. doi:10.1021/acs.biochem.6b01088

Tanaka, Y., Suzuki, G., Matsuwaki, T., Hosokawa, M., Serrano, G., Beach, T. G., . . . Nishihara, M. (2017). Progranulin regulates lysosomal function and biogenesis through acidification of lysosomes. *Hum Mol Genet, 26*(5), 969-988. doi:10.1093/hmg/ddx011

Ungurs, M. J., Sinden, N. J., & Stockley, R. A. (2014). Progranulin is a substrate for neutrophil-elastase and proteinase-3 in the airway and its concentration correlates with mediators of airway inflammation in COPD. *Am J Physiol Lung Cell Mol Physiol, 306*(1), L80-87. doi:10.1152/ajplung.00221.2013

Uversky, V. N. (2017). Protein intrinsic disorder-based liquid–liquid phase transitions in biological systems: Complex coacervates and membrane-less organelles. *Advances in Colloid and Interface Science, 239*, 97-114. doi:https://doi.org/10.1016/j.cis.2016.05.012

Van Damme, P., Van Hoecke, A., Lambrechts, D., Vanacker, P., Bogaert, E., van Swieten, J., . . . Robberecht, W. (2008). Progranulin functions as a neurotrophic factor to regulate neurite outgrowth and enhance neuronal survival. *The Journal of cell biology, 181*(1), 37-41. doi:10.1083/jcb.200712039

Van Damme, P., Van Hoecke, A., Lambrechts, D., Vanacker, P., Bogaert, E., van Swieten, J., . . . Robberecht, W. (2008). Progranulin functions as a neurotrophic factor to regulate neurite outgrowth and enhance neuronal survival. *The Journal of cell biology, 181*(1), 37-41. doi:10.1083/jcb.200712039

van der Zee, J., Le Ber, I., Maurer-Stroh, S., Engelborghs, S., Gijselinck, I., Camuzat, A., . . . Van Broeckhoven, C. (2007). Mutations other than null mutations producing a pathogenic loss of progranulin in frontotemporal dementia. *Hum Mutat, 28*(4), 416. doi:10.1002/humu.9484

Van Treeck, B., Protter, D. S. W., Matheny, T., Khong, A., Link, C. D., & Parker, R. (2018). RNA self-assembly contributes to stress granule formation and defining the stress granule transcriptome. *Proceedings of the National Academy of Sciences, 115*(11), 2734. doi:10.1073/pnas.1800038115

Wang, C., Duan, Y., Duan, G., Wang, Q., Zhang, K., Deng, X., . . . Fang, Y. (2020). Stress Induces Dynamic, Cytotoxicity-Antagonizing TDP-43 Nuclear Bodies via Paraspeckle LncRNA NEAT1-Mediated Liquid-Liquid Phase Separation. *Mol Cell, 79*(3), 443-458.e447. doi:https://doi.org/10.1016/j.molcel.2020.06.019

Wang, H. Y., Wang, I. F., Bose, J., & Shen, C. K. (2004). Structural diversity and functional implications of the eukaryotic TDP gene family. *Genomics, 83*(1), 130-139. doi:10.1016/s0888-7543(03)00214-3

Wang, J., Choi, J.-M., Holehouse, A. S., Lee, H. O., Zhang, X., Jahnel, M., . . . Hyman, A. A. (2018). A Molecular Grammar Governing the Driving Forces for Phase Separation of Prion-like RNA Binding Proteins. *Cell, 174*(3), 688-699.e616. doi:https://doi.org/10.1016/j.cell.2018.06.006

Ward, M. E., Chen, R., Huang, H. Y., Ludwig, C., Telpoukhovskaia, M., Taubes, A., . . . Green, A. J. (2017). Individuals with progranulin haploinsufficiency exhibit features of neuronal ceroid lipofuscinosis. *Sci Transl Med, 9*(385). doi:10.1126/scitranslmed.aah5642

Watanabe, S., Inami, H., Oiwa, K., Murata, Y., Sakai, S., Komine, O., . . . Yamanaka, K. (2020). Aggresome formation and liquid–liquid phase separation independently induce cytoplasmic aggregation of TAR DNA-binding protein 43. *Cell Death & Disease, 11*(10), 909. doi:10.1038/s41419-020-03116-2

Wheeler, J. R., Matheny, T., Jain, S., Abrisch, R., & Parker, R. (2016). Distinct stages in stress granule assembly and disassembly. *eLife, 5*, e18413. doi:10.7554/eLife.18413

Wright, P. E., & Dyson, H. J. (2015). Intrinsically disordered proteins in cellular signalling and regulation. *Nature Reviews Molecular Cell Biology, 16*(1), 18-29. doi:10.1038/nrm3920

Xiao, S., Sanelli, T., Chiang, H., Sun, Y., Chakrabartty, A., Keith, J., . . . Robertson, J. (2015). Low molecular weight species of TDP-43 generated by abnormal splicing form inclusions in amyotrophic lateral sclerosis and result in motor neuron death. *Acta Neuropathol, 130*(1), 49-61. doi:10.1007/s00401-015-1412-5

Xue, C., Lin, T. Y., Chang, D., & Guo, Z. Thioflavin T as an amyloid dye: fibril quantification, optimal concentration and effect on aggregation. *Royal Society Open Science, 4*(1), 160696. doi:10.1098/rsos.160696

Yang, P., Mathieu, C., Kolaitis, R.-M., Zhang, P., Messing, J., Yurtsever, U., . . . Taylor, J. P. (2020). G3BP1 Is a Tunable Switch that Triggers Phase Separation to Assemble Stress Granules. *Cell, 181*(2), 325-345.e328. doi:https://doi.org/10.1016/j.cell.2020.03.046

Zhang, T., Du, H., Santos, M. N., Wu, X., Reinheckel, T., & Hu, F. (2021). Differential regulation of progranulin derived granulin peptides. *bioRxiv*, 2021.2001.2008.425959. doi:10.1101/2021.01.08.425959

Zhang, Y.-J., Xu, Y.-F., Cook, C., Gendron, T. F., Roettges, P., Link, C. D., . . . Petrucelli, L. (2009). Aberrant cleavage of TDP-43 enhances aggregation and cellular toxicity. *Proceedings of the National Academy of Sciences, 106*(18), 7607. doi:10.1073/pnas.0900688106

Zhu, J., Nathan, C., Jin, W., Sim, D., Ashcroft, G. S., Wahl, S. M., . . . Ding, A. (2002). Conversion of proepithelin to epithelins: roles of SLPI and elastase in host defense and wound repair. *Cell, 111*(6), 867-878. doi:10.1016/s0092-8674(02)01141-8

SUPPLEMENTARY FIGURES

Figure S1

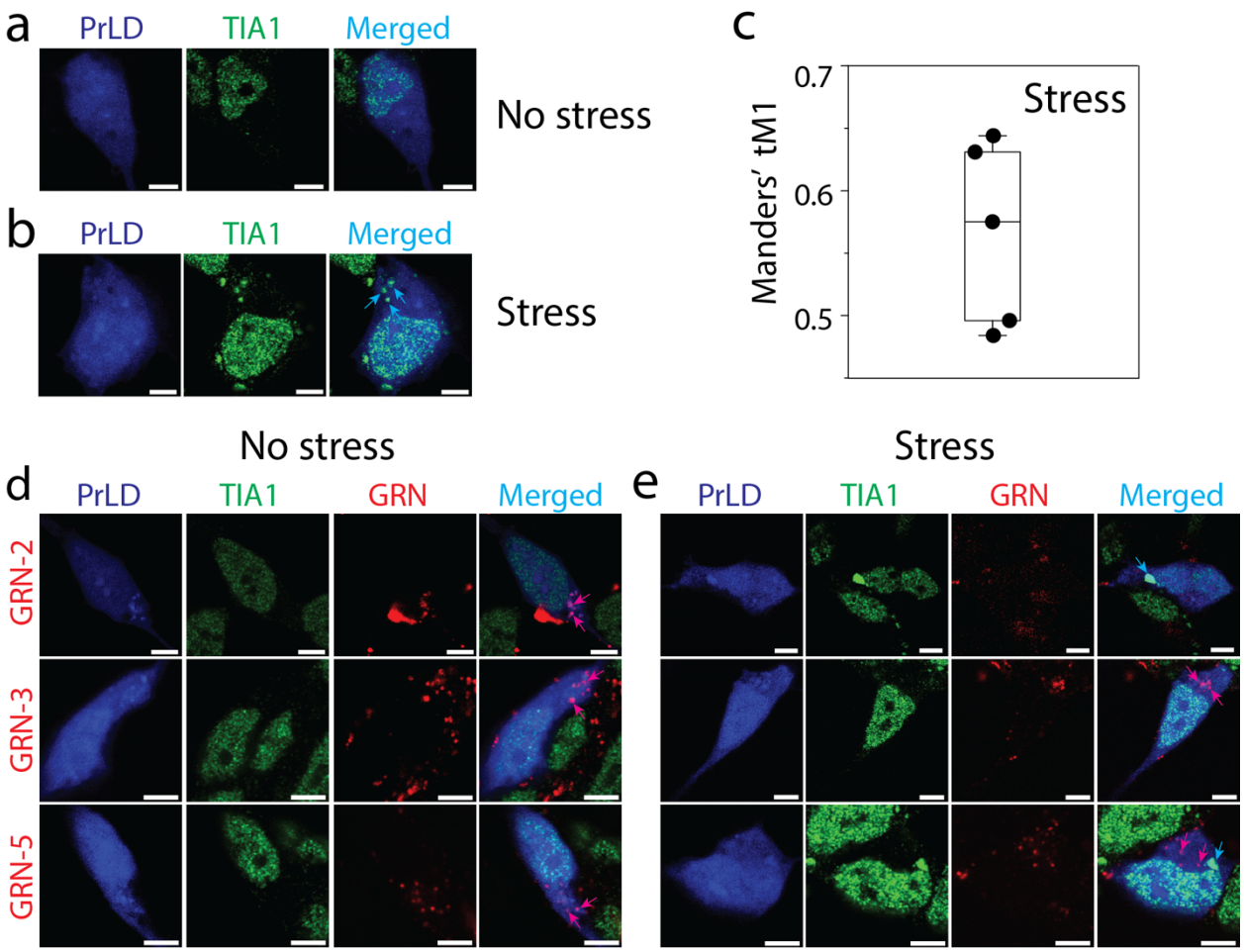

Figure S1. Localization of GRNs and PrLD within SGs. a-b) Immunofluorescence imaging of PrLD along with GRNs using TIA-1 antibodies with and without stress. PrLD-SBFP2 colocalization study with TIA1 in non-stressed cells (a) and sodium arsenite-induced stressed cells (b) (cyan arrows). C) Manders tM1 derived from five independently observed cells. d-e) Colocalization analysis of GRNs labeled with Hilyte-647 , PrLD and/or TIA-1 without stress (d) and with stress (e). Cyan colored arrows indicate the colocalization of PrLD and TIA1, while pink colored arrows represent colocalization of PrLD and GRNs. A three-way colocalization between GRN, PrLD and TIA1 was not observed. Scale bar represents 5 µm.

1150

1151 **Figure S2**

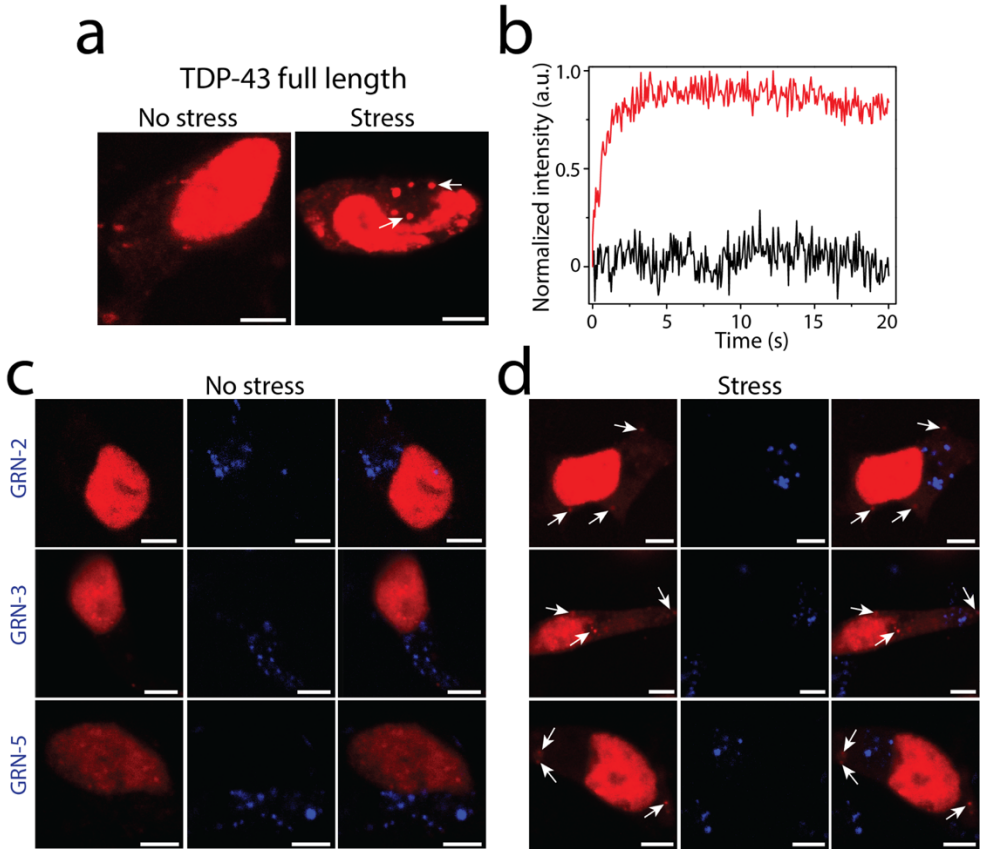

1152

1153 **Figure S2. Live cell analysis of SGs formed by full-length TDP-43 in SH-SY5Y cells.** Wild-type TDP43
1154 tdTomato with and without stress in SH-SY5Y cells (a). White arrows indicate the SGs formation in sodium
1155 arsenite treated cells. Normalized FRAP data of TDP-43 SGs and solid-like aggregates in sodium arsenite
1156 treated cells (—) and untreated cells (—) respectively. c-d) Confocal images of wtTDP43tdTomato
1157 transfected cells in presence of GRNs without (c) and with stress (d). Arrows in stressed cells indicate SGs
1158 containing TDP-43. No colocalization between GRNs and TDP-43 was observed. Scale bar represents 5
1159 µm.

1160

1161

1162

1163

1164

1165

Figure S3

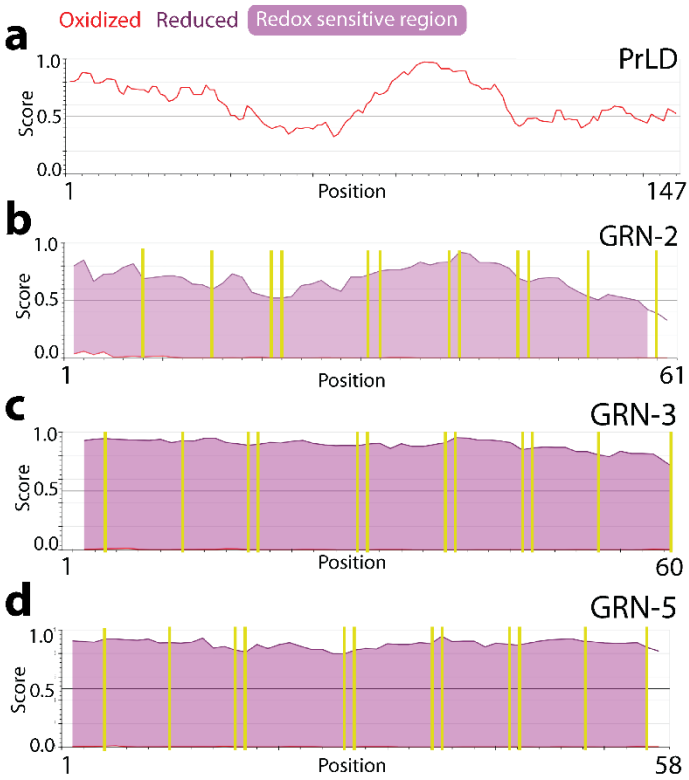

Figure S3. Redox-controlled disorder propensities of PrLD and GRNs. Structural disorder score of PrLD and GRNs estimated in a redox-dependent context using IUPred2A. Redox sensitive regions (shaded, purple) are calculated based on differences in disorder scores of the oxidized (red) and reduced (dark purple) forms of the proteins. Calculated scores above the 0.5 threshold signify disorder within the region. Cysteine residues are marked within the sequence of GRNs (yellow bars).

Figure S4

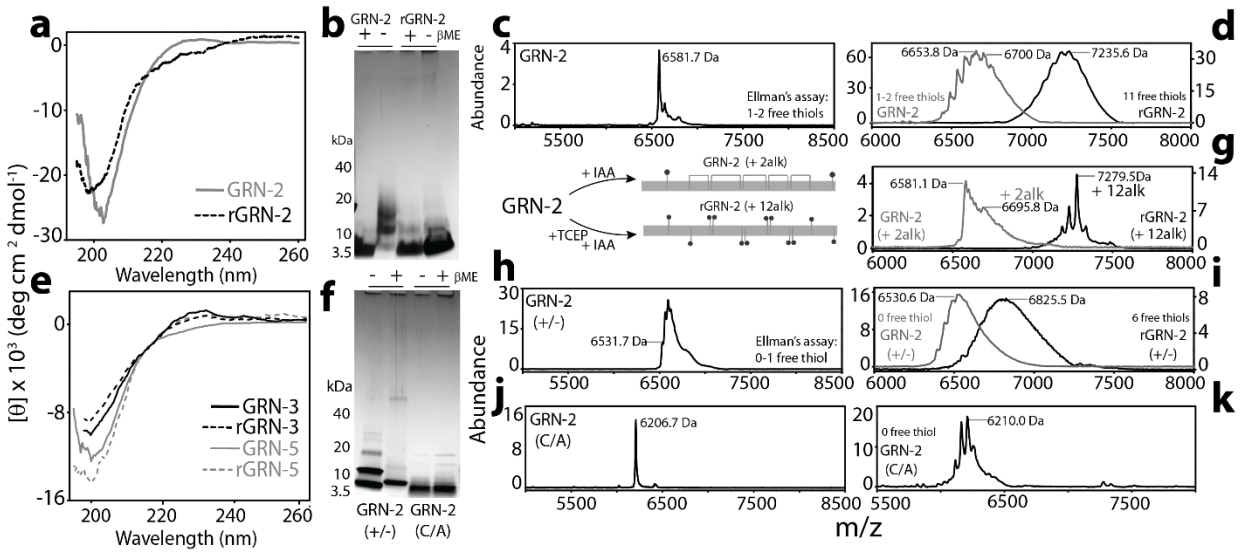

Figure S4. Biophysical characterization of GRNs. a) Far-UV circular dichroism (CD) spectra of GRN-2 and rGRN-2 displaying a characteristic profile of a structure dominated by random coils. b) SDS-PAGE analysis of GRN-2 and rGRN-2 the presence or absence of β-mercaptoethanol (βME) performed under denaturing conditions. c) MALDI-ToF MS graph of GRN-2 shows a peak at 6581.7 Da which corresponds to the monomeric form of the protein (theoretical mass: 6590.5 Da). Ellman's assay performed on the fraction reveals the presence of 1-2 free thiols. d) Free thiols in GRN-2 and rGRN-2 determined by alkylation with iodoacetamide and analyzed using MALDI-ToF MS. Alkylation of a free thiol by iodoacetamide leads to the addition of a thioether adduct (+ 59.0 Da). e) Far-UV CD spectra of the redox forms of GRN-3 and GRN-5. f) SDS-PAGE analysis of the mutant forms of GRN-2; GRN-2(+/-) and GRN-2(C/A) in the presence or absence of βME under denaturing conditions. g) Alkylated forms of GRN-2 were generated by either capping the two free-thiols in the oxidized form (GRN-2 2alk) or all twelve thiols in the reduced form (GRN-2 12alk) using iodoacetamide and were subsequently subjected to MALDI-ToF MS for analysis. h) Characterization of GRN-2(+/-) using MALDI-ToF MS shows a peak at 6531.7 Da corresponding to monomeric form of the protein (theoretical mass: 6536.4 Da). Two additional peaks were observed beside this corresponding to two, highly oxidized sulfur atoms in the cysteine (Sulfur-dioxide; +32 Da). Ellman's assay reveals the presence of about 1-free thiol in the protein i) Estimation of free thiols in the oxidized and reduced form of GRN-2(+/-) using alkylation assay. j) Characterization of GRN-2(C/A) using MALDI-ToF MS shows a peak at 6206.7 Da corresponding to monomeric form of the protein (theoretical mass: 6205.8 Da). k) Alkylation assay performed on GRN-2(+/-) analyzed using MALDI-ToF MS.

Figure S5

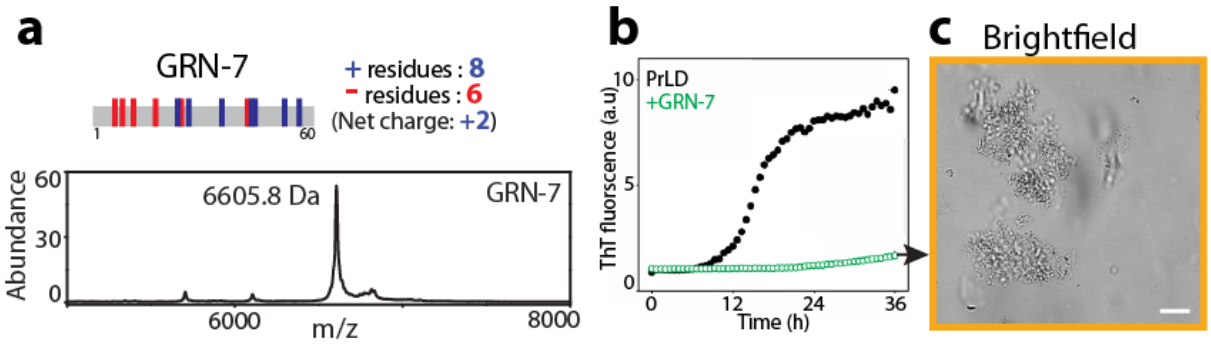

Figure S5. Interaction of GRN-7 with PrLD. a) Sequence of GRN-7 annotated with acidic and basic residues and the net charge at neutral pH. MALDI-ToF MS spectrum of oxidized GRN-7 shows a peak at 6605.8 Da corresponding to the monomeric protein (theoretical mass: 6615.4 Da). b) The effect of 40 μM GRN-7 on the aggregation of 20 μM PrLD was monitored in the presence of 15 μM ThT for a period of 36 h at 37ºC under quiescent conditions. c) DIC micrograph of the sample containing GRN-7 and PrLD from b) showing the presence of solid-aggregates (liquid-solid phase separation, saffron box). Scale bar represents 20 μm.

Figure S6

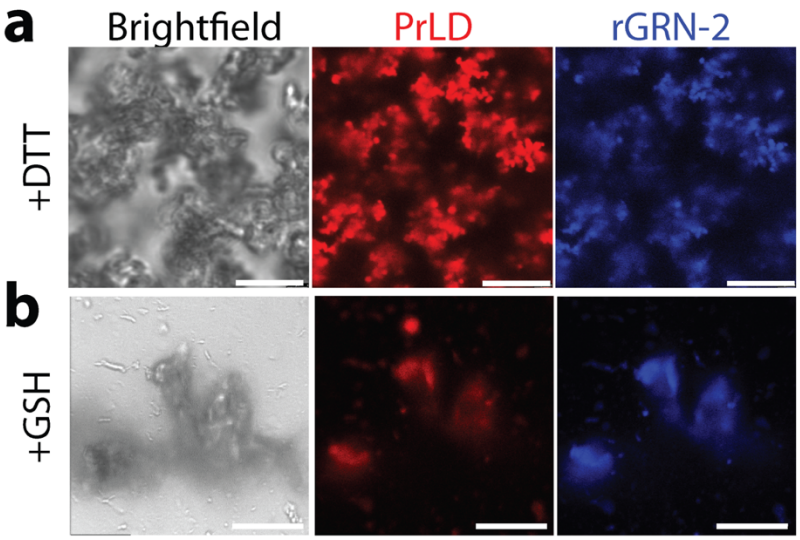

Figure S6. Reduction of GRN-2 with alternative reducing agents. a-b) Confocal micrographs of mixtures containing 20 μM PrLD with 40 μM rGRN-2 reduced using 12 molar excess of dithiothreitol (DTT) (a) or gluthathione (GSH) (b). Reactions contain 1% fluorophore labeled proteins for microscopic visualization. Reactions were initiated at room temperature and imaged within 15 minutes.

Figure S7

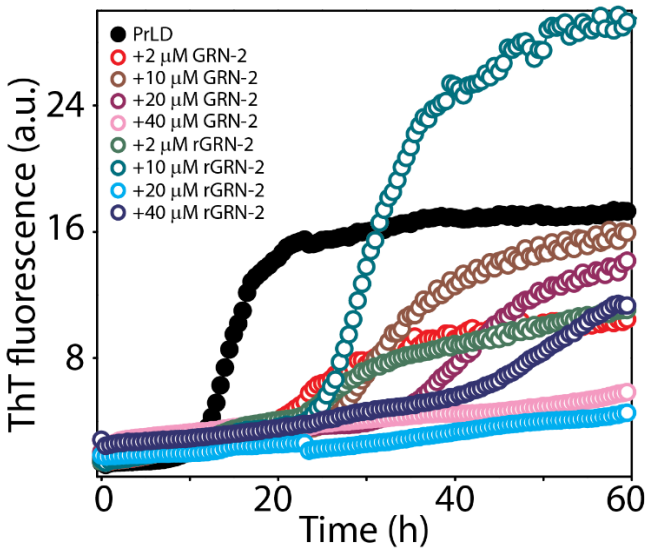

Figure S7. Formation of ThT-positive species of PrLD in presence of GRN-2. The amyloid formation of 20 μM TDP-43 PrLD alone (●) or in presence of varying concentrations (2-40 μM) of GRN-2 or rGRN-2, buffered in 20 mM MES, pH 6.0, monitored using 15 μM ThT for a period of 60 h at 37 ºC under quiescent conditions.

Figure S8

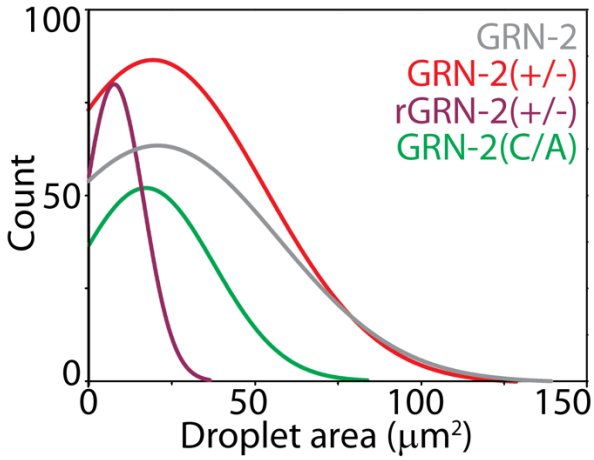

Figure S8. Comparison of the droplet area distributions of GRN-2 and its mutants. Micrographs of reactions depicted in Fig 5 were subjected to droplet area distribution analysis as described previously using the imageJ platform. Samples of 20 μM PrLD with 40 μM GRN-2 (gray), GRN-2(+/-) (red), rGRN-2(+/-) (purple) and GRN-2(C/A) (green) were considered for analysis with a minimum of 100 droplets enumerated. The normal distribution curves for each sample depicted were generated using Origin 8.5 graphing software.